A ^{57}Fe Mössbauer study on the thermal oxidation of iron in biotite mica

by

Pamela Tume

Thesis submitted to the School of Graduate Studies
of the University of Ottawa in partial fulfilment
of the requirements for the degree of
Master of Science in Physics

Physics Department
Faculty of Science
University of Ottawa
Ottawa, Canada
1992

ISBN 0-315-80016-X

UNIVERSITÉ D'OTTAWA
UNIVERSITY OF OTTAWA

Abstract

We have studied the oxidation in air of a well characterized biotite sample. Large single crystal wafers were annealed at various temperatures up to 875°C and for various times up to 94 hours.

The oxidation proceeds primarily via the oxyannite reaction:

$$(Fe^{2+} + OH^{-})_{mica} \rightarrow (Fe^{3+} + O^{2-})_{mica} + H$$

and was therefore conveniently followed by ^{57}Fe Mössbauer spectroscopy, which resolves the 2+ and 3+ valence states of iron.

Room temperature Mössbauer absorption spectra were measured at normal incidence to the ab-plane for samples annealed at various temperatures for 24 hours and for samples annealed at 732°C for various times. The analysis is non-trivial due to overlapping ion-specific subspectral contributions and the added difficulty of texture effects from the single crystal absorbers. Mössbauer thickness effects were also considered and were found to have a negligible impact on the extracted Fe^{3+}/Fe^{2+} amounts.

The main features of the annealing time and temperature dependencies of the Fe^{3+}/Fe^{2+} amounts are understood in terms of a simple model in which: (i) the overall oxidation reaction proceeds homogeneously via a time-wise bottleneck step that follows a classic thermal activation law

and (ii) a certain fraction of the original Fe^{2+} is inaccessible to the oxidation reaction.

The resulting barrier energy, $E_b = 2.36^{+.01}_{-.02}$ eV is in the range of measured barrier energies for dehydroxylation of layer silicates. This suggests that the bottleneck step may be local dehydroxylation:

$$(OH^- \rightarrow O^{2-} + H^+)$$

The persistent Fe^{2+} can be understood from local crystal-chemical considerations.

Acknowledgments

During this project I have received support from many different people. At this time I would like to especially thank Dr. D. Rancourt for his invaluable assistance with the interpretation of the Mössbauer results and for reviewing this manuscript. I also owe a debt of gratitude to Dr. A. Lalonde for his help in understanding the crystal chemistry of micas and for providing the single-crystal biotite sample with the sample's microprobe analyses. Finally, I would like to express my appreciation for the support of my friends, in particular my husband Vince, over the period of my studies. This work was financially supported by the Natural Sciences and Engineering Research Council of Canada.

TABLE OF CONTENTS

List of Abbreviations and Symbols

A_i, A_p, A_{2+}, A_{3+}	spectral area assigned to the i^{th} family of crystallographic sites, spectral area of observed peak p, area of an Fe^{2+} subspectrum, area of an Fe^{3+} subspectrum
A_{th}	thickness corrected spectral area of an observed peak
A_{total}	total area of a spectrum
A-B-C	notation used to describe a particular model having a specified number of lines in observed peaks A, B and C
BG	background of a spectrum
C_k	number of gamma rays counted in the k^{th} velocity channel
χ^2, χ_{red}^2	chi-squared, reduced chi-squared
δ	center shift parameter of a quadrupole doublet
Δ	quadrupole splitting parameter
$D(\psi)$	elemental Lorenztian quadrupole doublet
E_B	barrier energy
f	rate constant
f_a, $f_{a,i}$	absorber recoil-free fraction; absorber recoil-free fraction for the i^{th} site

f_o	attempt frequency
Fe^{2+}/Fe_{total}	ratio of the number of Fe^{2+} atoms divided by the total number of iron atoms (in the absorber)
Fe^{3+}/Fe_{total}	ratio of the number of Fe^{3+} atoms divided by the total number of iron atoms (in the absorber)
FWHM	full width at half height maximum
γ	FWHM of a Lorentzian line
Γ_o	natural FWHM of an emission line
$G(\psi)$	Gaussian distribution function, normalised to unit area
h_i, h_k	Lorentzian height of the i^{th} Voigt line, Lorentzian height of one of the two lines (k=+1,-1) of an elemental quadrupole doublet
$h/2\pi$	Planck's constant divided by 2π
$I_{1/2}$, $I_{3/2}$	nuclear spin quantum number (I) of the ground state, and first excited state, respectively, for ^{57}Fe
k_B	Boltzmann's constant
$L(\psi-z)$, $L(a;\psi)$	single Lorenztian line centered upon velocity z; single Lorenztian line described by the components of the multidimensional; vector a and the argument ψ
m_I	magnetic spin quantum number assigned to the substates of I

M1	a trans octahedral site
M2	a cis octahedral site
MOC2661	label that identifies our particular natural biotite
MS	Mössbauer spectroscopy
ν	number of degrees of freedom for a least squares fit of a particular model
$n_{a,i}$	number of iron probe nuclei assigned to the i^{th} family of sites in the absorber
n_a	total number of iron probe nuclei in the absorber
N_{2+},N_{3+}	amount of Fe^{2+}, and Fe^{3+}, respectively, in a biotite sample that has been annealed for a specific time and temperature
N_{2+}^0, N_{3+}^0	amount of Fe^{2+}, and Fe^{3+}, respectively, in a virgin state sample of our biotite
N_{Fe}	total amount of iron in an annealed biotite sample
$N(\psi)$, $N(a;\psi)$	theoretical lineshape of a spectrum, theoretical lineshape described by the components of the multidimensional; vector a and the argument ψ
O	octahedral layer of the basic composite sheet of mica
R_{2+}	ratio of the low energy to high energy lines of an Fe^{2+} suspectrum
R_{3+}	ratio of the low energy to high energy lines of an Fe^{3+} suspectrum

RT	room temperature (22°C)
$\sigma_{a,i}$	normalised, absorber cross section for the i^{th} site
σ_i	Gaussian width of the i^{th} Voigt line (σ= Gaussian FWHM/ $(2\sqrt{2\ln 2})$)
σ_o	resonance cross section for the 14.4 keV ^{57}Fe Mössbauer transition
SCA	single channel analyzer
τ	decay time of an excited state
t, t_{AN}	annealing time, in hours
t_a	absorber thickness parameter
T, T_{AN}	annealing temperature, in degrees Celsius or Kelvin
T	tetrahedral layer of the basic composite sheet of mica
TGA	thermogravimetric analysis
$V(\psi)$	Voigt lineshape which corresponds to a Gaussian distribution (normalised to 1) of Lorentzian lines
w_i	center position of a Voigt line
X	interlayer cation in the ideal formula unit of mica
ψ	velocity channel, or gamma ray energy
Y	octahedral cation in the ideal formula unit of mica
Z	tetrahredral cation in the ideal formula unit of mica

List of Figures

page

List of Tables

In the text: page

In Appendix A:

Introduction

This thesis is a preliminary study of the kinetics of iron oxidation in biotite mica using ^{57}Fe Mössbauer spectroscopy. In this study room temperature spectra were collected on single crystal wafers heated in air to various temperatures and for various times. Resulting Fe^{2+} and Fe^{3+} relative populations were determined using a novel spectral interpretation that took into account the single crystal nature of the absorber.

The difficulties posed by overlapping Fe^{2+} and Fe^{3+} quadrupole doublets were overcome by considering that each biotite spectrum had a well defined, high energy Fe^{2+} line. Consequently, assuming a constant ratio of low energy to high energy Fe^{2+} line intensities allowed us to determine the Fe^{2+} and Fe^{3+} populations for each annealed biotite.

Previous authors have studied the oxidation of mica powders or have used powdered absorbers (e.g. Gendler et al, 1978). The oxidation of a powder may be fundamentally different from that of a large single crystal. The former will have size dependencies whereas the latter will be an intrinsic property of the material.

Earlier oxidation studies (e.g. Hogg and Meads, 1975) on different biotite compositions have indicated that Fe^{2+} will completely oxidize into Fe^{3+} prior to thermal decomposition of the biotite structure. However, in this

study we find that a small but significant amount of Fe^{2+} remains unoxidized. This suggests that iron oxidation in biotite is sensitive to the local chemical and crystallographic environment.

Understanding the time-temperature dependence of iron oxidation in mica provides a clearer picture of weathering in a rock outcrop containing the mica specimen (Bailey, 1984). It is important to know if and on which time scale a mica will evolve after its original crystallization because mica is used as a probe of the crystallization conditions when it can be assumed that it has not been altered. This and other geological applications motivate this study.

2. Mica: Structure, Nomenclature and Oxidation

2.1 Crystal chemistry and nomenclature

The ideal chemical formula unit for the layer silicate mineral mica is:

$$XY_{2\text{ or }3}Z_4O_{10}(OH)_2 \qquad (1)$$

where X, Y, and Z correspond, respectively, to the interlayer, octahedral, and tetrahedral cations. Here, O represents oxygen.

A common structural feature found in all micas is the basic composite sheet (or T-O-T layer) composed of two tetrahedral (T) layers surrounding one octahedral (O) layer (see figure 1). Each T layer is formed by adjacent tetrahedra sharing their basal oxygen ions. This linking forms a hexagonal mesh in the pattern of the T bases. The fourth T apex, perpendicular to the mesh, is shared with an octahedral oxygen ion. The two T layers are staggered relative to each other. The remaining vacant O apices are individually filled with single hydroxyl groups that are located below the centre of the 6-fold T rings. Adjacent composite sheets are electrostatically bound to each other by the interlayer cations.

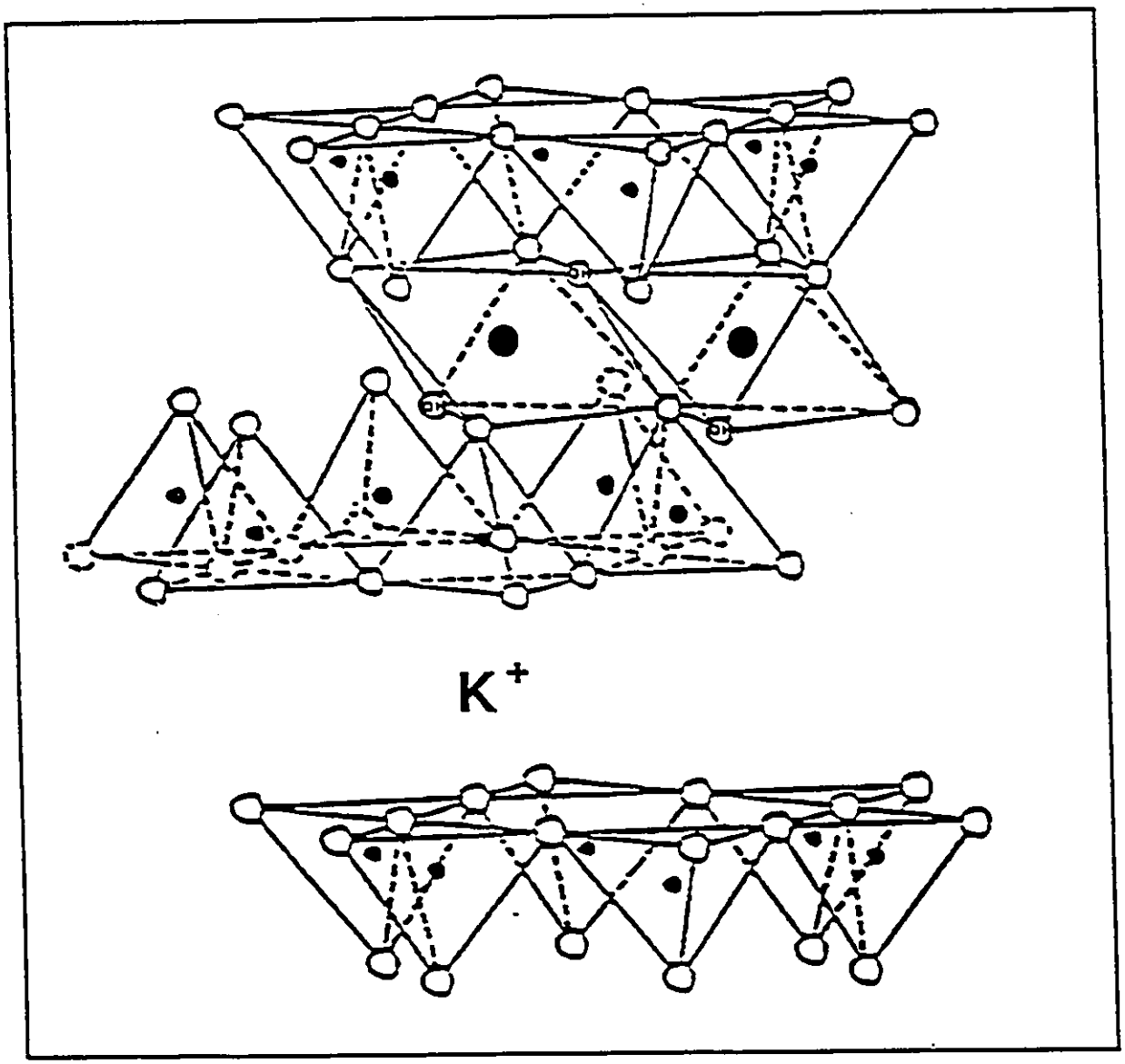

Fig. 1 T-O-T layer

Schematic of the octahedral (O) and tetrahedral (T) sites in a 2:1 layered silicate. Small filled circles are cations in T sites, large filled circles are cations in O sites, and open circles are oxygen. The open circles labelled by OH- are hydroxyl groups. K+ represents the interlayer cation content between adjacent T-O-T layers

The mica family can be classified into two main groups depending upon the T-O-T sheet charge per formula unit (x). The true micas ideally have x = -1.0 which is balanced by mostly monovalent interlayer cations such as K^+ and Na^+. The brittle micas compensate their x = -2.0 with divalent interlayer cations like Ca^{2+} and Ba^{2+}. In true micas the T sites are commonly filled with Si^{4+} and Al^{3+} in a 3:1 ratio. Brittle micas however, have a less consistent Si^{4+}: Al^{3+} occupancy.

The two main groups can be subdivided based upon the filling of the O sites. There are three distinct crystallographic O sites that can be distinguished by the arrangement of their hydroxyl apices (see figure 2). The two hydroxyl groups of the M1 site, or trans arrangement, occupy the furthest opposed apices of the octahedral cage (C_2 or 2 point symmetry). The other two sites are both M2 or cis sites (C_{2h} or 2/m point symmetry) and share two hydroxyl apices on a common edge. These O sites may be occupied by a wide variety of cations, such as Mn^{2+}, Mg^{2+}, Fe^{2+}, Fe^{3+}, Al^{3+}, and others. If all three different O sites are filled, the mica is called trioctahedral, whereas if only two of the O sites are filled the mica is called dioctahedral.

The field of true trioctahedral mica can be divided into species, based upon the relative amounts of Fe^{2+} and Mg^{2+}, the most common O cations. The annite species is the iron-rich end member ideally having iron in all O sites. Biotite is the intermediate case of iron solid solution with

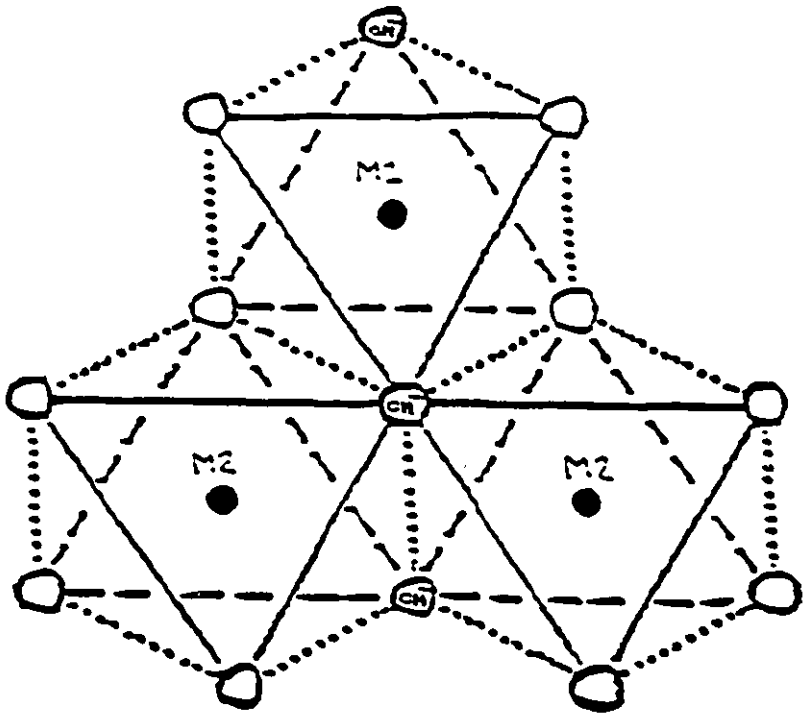

Fig. 2 Cis/ Trans octahedral sites

Illustration of the trans (M1) and cis (M2) sites in the octahedral layer of a 2:1 layered·silicate. The filled circles are O site cations, open circles are oxygen, and open circles labelled by OH- are hydroxyl groups. The solid lines are the top triangular faces of the octahedra and the dashed lines are the bottom triangular faces.

$Fe / (Fe + Mg) > 0.33$. The phlogopite species is iron-poor with $Fe / (Fe+Mg) < 0.33$. The ideal end member with only Mg occupying the O sites is also called phlogopite.

Further information on the chemical and physical properties of the mica family can be obtained in the literature. General introductions to the chemistry and structure of mica have been written by Deer et al (1966) and Zoltai and Stout (1984). For a more detailed review concerning the geological and mineralogical aspects of mica, the reader is referred to a monograph edited by S.W. Bailey (1984).

2.2. Oxidation of iron in biotite

In biotite, the oxidation of O site Fe^{2+} into Fe^{3+} is known to be sensitive to environmental conditions such as temperature and oxygen availability. Two possible processes by which iron oxidation may occur are exfoliation (the loss of interlayer cations) and the loss of hydrogen from hydroxyl groups. These reactions are given below for the annite species (e.g. Addison et al, 1962; Rimsaite, 1967; Farmer et al, 1971).

.exfoliation (in the presence of water):

$$(Si_3AlO_{10})Fe^{2+}{}_3(OH)_2K + {}^1/_4\, O_2 + {}^1/_2H_2O \longrightarrow$$

$$(Si_3AlO_{10})\, Fe^{2+}{}_2Fe^{3+}(OH)_2 + KOH \qquad (2)$$

.exfoliation (in the absence of water):

$$(Si_3AlO_{10})Fe^{2+}{}_3(OH)_2K + {}^1/_4\, O_2 \longrightarrow$$

$$(Si_3AlO_{10})\, Fe^{2+}{}_2Fe^{3+}(OH)_2 + {}^1/_2\, K_2O \qquad (3)$$

.loss of hydrogen (in the presence of oxygen):

$$(Si_3AlO_{10})\, Fe^{2+}{}_3(OH)_2K + {}^1/_2\, O_2 \longrightarrow$$

$$(Si_3AlO_{10})\, Fe^{2+}Fe^{3+}{}_2O_2\, K + H_2O \qquad (4)$$

loss of hydrogen (in the absence of oxygen):

$$(Si_3AlO_{10})\,Fe^{2+}{}_3(OH)_2K \longrightarrow (Si_3AlO_{10})Fe^{2+}Fe^{3+}{}_2O_2K + H_2 \qquad (5)$$

The main iron oxidation process that is expected to dominate under mild oxidation conditions is considered to be the loss of hydrogen from hydroxyl groups, the net result being:

$$(\ Fe^{2+} + OH^-\ )_{mica} \rightarrow (\ Fe^{3+} + O^{2-}\ )_{mica} + H. \qquad (6)$$

For each O site Fe^{2+} that becomes O site Fe^{3+}, one O apex hydroxyl group dissociates to leave both an O apex O^{2-} in it's place and a free neutral hydrogen atom. The latter hydrogen participates in making either H_2O (reaction (4)) or H_2 (reaction (5)), thereby supplying the driving force and making the overall reactions exothermic.

Other authors (Hogg and Meads, 1975) have found that oxygen is required for significant oxidation to occur. This suggests that under mild conditions (i.e., relatively low temperatures) reaction (4) dominates.

In terms of the microscopic mechanism that is responsible for the dynamics of the reaction, several scenarios are possible. For example,

hydroxyl may first dissociate leaving hydrogen that diffuses to the surface where it reacts with O_2 gas to give H_2O (Addison et al, 1962).

In all multi-step mechanisms we expect one step might dominate the dynamics with its largest barrier energy. This is because the slowest step would act as a bottleneck for the time dependence. We might then hope to analyze both our time series data and our temperature series data (see sections 5.1 and 5.2) using the simplest possible model:

$$N_{3+} = N_{3+}^{\circ} + N_{2+}^{\circ} \left(1 - \exp(-ft) \right) \tag{7}$$

$$N_{2+} = N_{2+}^{\circ} \exp(-ft) \tag{8}$$

$$N_{2+}^{\circ} + N_{3+}^{\circ} = N_{2+} + N_{3+} = N_{Fe} \tag{9}$$

$$f = f_o \exp(-E_b / k_B T) \tag{10}$$

where N_{2+}° and N_{3+}° are respectively the original Fe^{2+} and Fe^{3+} amounts (as found in an unoxidized biotite sample), N_{Fe} is the total amount of O site Fe, E_b is the bottleneck barrier energy, f is the rate constant, f_o is the bottleneck step attempt frequency, k_B is the Boltzman constant, and T is the annealing temperature in Kelvin. The time t is the total time that the sample was annealed at temperature T.

In this thesis we shall assume that the net reaction (6) dominates in our biotite sample and under our reaction conditions. This is consistent with all our observations and implies that a one to one correspondence exists between each Fe^{2+} to Fe^{3+} event, as measured by Mössbauer, and the loss of one H. In addition we examine the validity of equations (7) and (8).

Finally, let us briefly review some of the literature concerning the possible oxidation reactions under different conditions and with different mica samples. The availability of oxygen does not necessarily control the oxidation of iron in biotite. Certain authors (Tripathi et al, 1978) consider that regardless of the presence of oxygen, reaction (5) is considered the principle oxidation reaction under low temperature conditions. Further temperature increases, in an oxygenated environment, will cause additional Fe^{3+} to form along reaction (4) up to the point of decomposition, at approximately 900°C (Hogg and Meads, 1975).

The loss of octahedral iron has also been proposed as a method for iron oxidation. Hydrothermal biotite oxidation studies have observed the formation of hematite at temperatures as low as 350°C, without breaking down the biotite structure (Hellner and Euler,1957). However, other thermal oxidation studies on biotite suggest the formation of hematite is insignificant for temperatures below 900°C (Hogg and Meads, 1975).

During heating of the biotite lattice, iron oxidation begins before the loss of structural hydroxyl groups by dehydroxylation. The dehydroxylation process in biotite is thought to occur at temperatures above 500°C and involves condensation of two hydroxyl groups across a vacant O site to produce water and a structural oxygen anion. Any structural hydrogen that is not loss during either dehydroxylation or iron oxidation is thought to remain in the biotite until structural breakdown of the T-O-T layers (Vedder and Wilkins, 1969).

2.3 Suitability of Mössbauer to quantify iron oxidation

To quantify the degree of iron oxidation in biotite, we must resolve the valence states of iron and estimate their corresponding populations in the sample. Mössbauer Spectroscopy (MS) is an established microscopic technique which is sensitive to both the nature of the probe ion (valence state) and the symmetry of its chemical bonding (see Greenwood and Gibb, 1971). ^{57}Fe is the most widely used Mössbauer isotope and ^{57}Fe MS provides a convenient and reliable non-destructive method of "in situ" Fe^{2+} and Fe^{3+} analysis.

The information obtained by MS is not easily obtained by other analysis techniques. X-ray diffraction is a standard technique used to determine the sample's structure, but it is unable to distinguish between Fe^{2+} and Fe^{3+} ions in the lattice. Chemical analysis does attempt to determine the relative Fe^{2+} and Fe^{3+} amounts, unfortunately the results are not always consistent (Annersten,1974; Bancroft and Brown,1975; Goodman and Wilson,1973).

The main Mössbauer results can also be supplemented by thermogravimetric analysis (TGA). However, performing TGA on a biotite is complicated since the change in sample mass may be attributed to several processes such as oxidation, dehydroxylation, exfoliation or even the formation of trapped oxides.

3. Mössbauer Background

3.1 Hyperfine parameters related to an elemental spectrum in a non-magnetically-ordered material

The fundamental physical mechanism that makes Mössbauer spectroscopy possible is the Mössbauer effect (Mössbauer, 1958). In summary, certain excited nuclei bound to a lattice can emit (or absorb) gamma radiation without recoil of the nucleus.

By Doppler shifting the energy of the thus emitted photons, it is possible to scan a narrow range of photon energies. Exposing a material that contains the same Mössbauer nuclei as the emitter to this energy scan produces an absorption spectrum for this sample. The characteristics of the spectrum depend on the hyperfine interactions between the absorbing nuclei and their local electronic and magnetic environments. A particular electronic environment corresponding to a particular crystallographic site causes specific hyperfine interactions that determine the precise nuclear energy level diagram of the Mössbauer isotope on that site.

This leads to the definition of an elemental contribution to the Mössbauer spectrum. An elemental spectrum arises from the recoilless resonant absorbtion of gamma radiation by probe nuclei in identical electronic (i.e., chemical, crystallographic and magnetic) environments.

For a non-magnetically-ordered material, the elemental spectrum corresponding to the 14.4 keV transition in ^{57}Fe must consist of two Lorentzian shaped absorption lines. Such a "doublet" is characterized by a centre shift (δ) and a quadrupole splitting (Δ) (e.g., Greenwood and Gibb, 1971). In figures 3a and 3b, a typical elemental quadrupole doublet is shown and its corresponding nuclear energy level diagram, respectively. The δ references the centre between the two absorption lines with respect to a standard absorber. The Δ is the measured separation between the two resonance lines of the particular spectrum. Both δ and Δ are energies (or gamma ray frequencies) given in units (mm/sec) of the Doppler velocities used to produce the incident radiation. For ^{57}Fe 1 mm/sec = 4.8074×10^{-8} eV.

The main cause of the spectrum's centre shift (δ) is the electric monopole interaction between the charge on the nucleus and the s-electron density at the nucleus. This coulombic interaction alters the nuclear energy separation of the levels involved in the Mössbauer

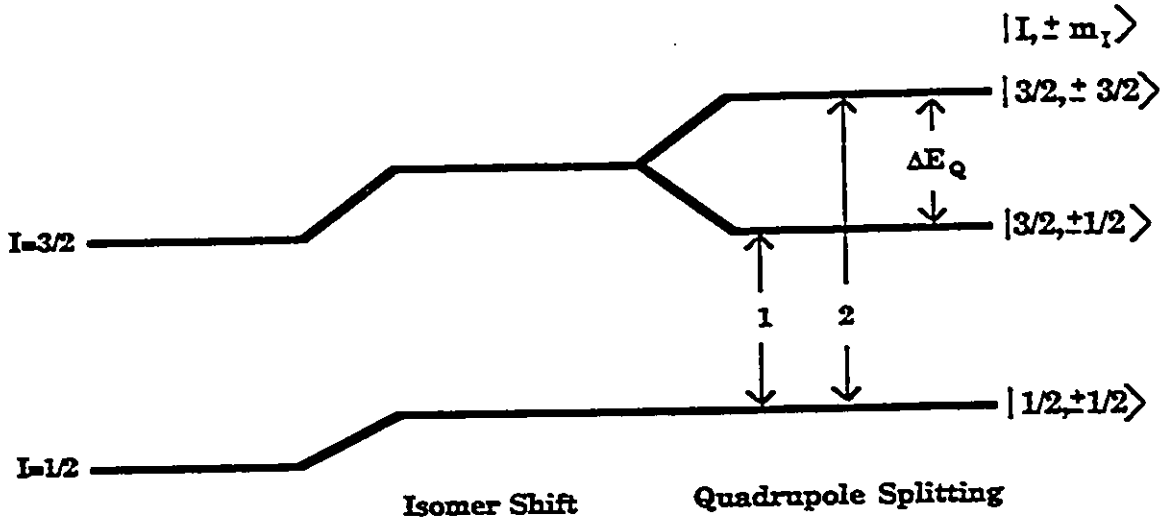

Fig. 3a ^{57}Fe nuclear level diagram including the ground and quadrupole split first excited state

The first excited state has nuclear spin quantum number, I, equal to 3/2 and is split into two degenerate sublevels. Each sublevel is labelled by its respective magnetic spin quantum number, m_I. The magnitude of the energy separation, ΔE_Q, between the first excited state sublevels is equal to the magnitude of the quadrupole splitting parameter Δ. The ground state ($I=1/2$, $m_I = \pm 1/2$) is not split, since it has zero nuclear quadrupole moment.

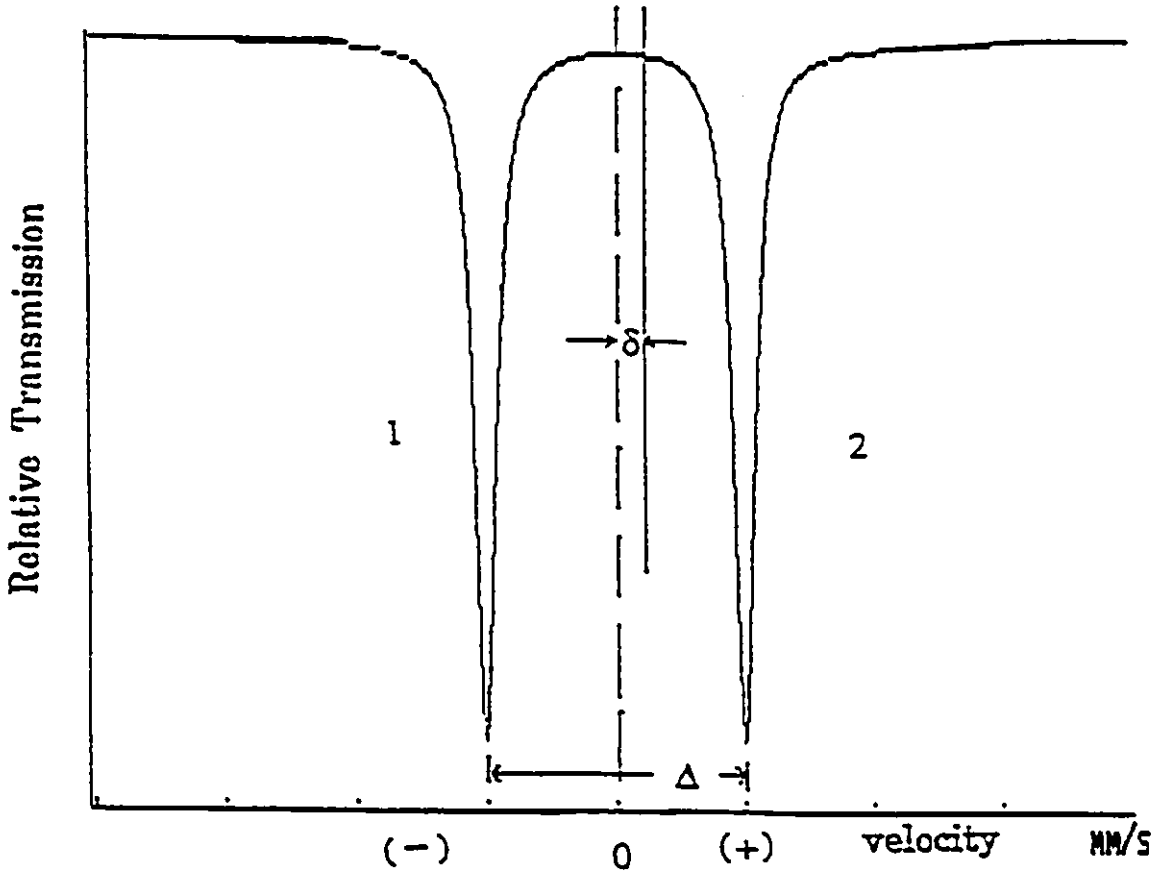

Fig 3b

An elemental quadrupole doublet spectrum for ^{57}Fe probe nuclei that is based upon the energy level diagram of figure 3a. There are two possible Mössbauer transitions : between each of the first excited state sublevels and the ground state. The numbered transitions, i.e. 1 and 2 in figure 3a, give rise to the corresponding resonance absorption lines in the elemental doublet as shown in this figure. Transitions line 2 is centered about a higher velocity than line 1, since line 2 has a larger magnitude of transition energy than line 1. The center shift, δ, of this elemental spectrum is the sum of the isomer shift and a temperature dependent second order Doppler shift.

transition. The electric quadrupole interaction, between the electric field gradient at the nucleus and the nuclear quadrupole moment, determinesthe magnitude of the quadrupole splitting (Δ).

The relative absorption line intensities, or depths or heights, in a quadrupole doublet are sensitive to the direction of the incident radiation with respect to the electric field gradient at the nucleus. On the other hand, changing the orientation of a randomly packed, powdered absorber, will not affect the heights of the resonance lines, due to random orientation of many small crystals.

The lineshape of the elemental quadrupole spectrum is the sum of two Lorentzian lines, which can be written as:

$$D(\psi) = BG - \sum_{k=1,-1} L\left(\delta + k\frac{\Delta}{2},\ \gamma,\ h_k;\ \psi \right) \qquad (11)$$

where ψ is the γ-ray energy (in mm/s) and BG is the background as observed far away from all Mössbauer transitions. The Lorentzian function has the following form:

$$L\left(\delta + k\frac{\Delta}{2},\ \gamma,\ h_k;\ \psi \right) = \frac{h_k \frac{\gamma^2}{4}}{\{ \psi - [\delta + k\frac{\Delta}{2}] \}^2 + \frac{\gamma^2}{4}} \qquad (12)$$

This describes a single Lorentzian line with height h_k, full width at half maximum (FWHM) γ, and centred on $[\delta+k\Delta/2]$. This Lorentzian profile was originally derived from quantum mechanics by Weisskopf and Wigner (1930).

The natural linewidth of the emission line can be obtained from the Heisenberg uncertainty relation as:

$$\Gamma_o \, \tau \quad = \quad \frac{h}{2\pi} \qquad (13)$$

Here, Γ_o is the natural FWHM of the emission line, τ is the decay time of the excited state and h is Planck's constant. The 14.4 keV Mössbauer transition in ^{57}Fe has a measured half-life of 97.7 ns. This results in a very narrowly defined emission line having a theoretical value of Γ_o = 4.67×10^{-9} eV (or 0.097 mm/sec). In elemental absorption spectra and in the absence of any experimental artifacts, the Lorentzian lines have γ = $2\,\Gamma_o$ = 0.194 mm/sec.

Since most minerals and materials have many non-equivalent crystallographic sites or local environments that are occupied by the Mössbauer probe nuclei, the Mössbauer spectrum of a non-magnetically-ordered material (in the absence of experimental artifacts such as finite absorber thickness) in general, consists of a superposition of elemental

doublets as described in this section. The lineshape of the sample's spectrum is the sum of the individual elemental lineshapes. While the intensity and width of an observed peak may vary, the FWHM of the observed line must be at least greater or equal to the natural FWHM of an elemental absorption line; that is, FWHM is greater or equal to $2\,\Gamma_o$.

3.2 Relationship between the number of absorbing nuclei and the spectral area

Although the individual elemental doublets in an observed spectrum cannot usually be resolved, it is possible to model the spectrum such that distinct sets or distributions or families of hyperfine parameters are determined. For convenience, the i^{th} family of sites is defined as those local electronic environments that characterize the i^{th} set of hyperfine parameters. Some further details used to model the spectra will be covered in sections 3.4 and 5.2.

For our purposes, the number of probe nuclei, per gram of absorber, associated with an i^{th} family of sites must be determined. The spectral, A_i, area for the i^{th} site is:

$$A_i = \int_{-}^{-} d\psi \sigma_{a,i}(\psi) = \frac{\pi n_{a,i} f_{a,i} \sigma_o \Gamma_o}{2} \qquad (14)$$

where σ_o is the resonance cross-section for the transition, $n_{a,i}$ is the number of probe ions associated with the i^{th} parameter set, per unit area of the absorber and $f_{a,i}$ is the absorber recoilless fraction. For mica at room temperature, f_a has an average non-valence specific value of approximately

0.7. Under the assumption that $f_a = f_{a,i}$, the ratio of the number of probe nuclei in the i^{th} family of sites to the total number of probe nuclei in the sample may be written as:

$$\frac{n_{a,i}}{n_a} = \frac{n_{a,i}}{\sum_j n_{a,j}} = \frac{\frac{1}{\pi\, f_{a,i}\, \sigma_o\, \Gamma_o}\int_{-\infty}^{\infty} d\psi\ \sigma_{a,i}(\psi)}{\frac{1}{\pi\, f_a\, \sigma_o\, \Gamma_o}\ \sum_j \int_{-\infty}^{\infty} d\psi\ \sigma_{a,j}(\psi)} \qquad (15)$$

where n_a is the total number of probe nuclei per unit area of the absorber. This may be simplified to:

$$\frac{n_{a,i}}{n_a} = \frac{A_i}{\sum_j A_j} = \frac{A_i}{A_{total}} \qquad (16)$$

where A_{total} is the total area of the absorption spectrum.

3.3 Discrimination of the ion-specific spectral contributions (or subspectra)

Mössbauer studies of compounds containing iron atoms in octahedrally coordinated oxygen environments (Fe_{oct}) have shown that a change in the valence state of the probe atom will affect the magnitudes of the center shift, δ, and quadrupole splitting, Δ (e.g. Greenwood and Gibb, 1971). Figure 4 is a plot of the room temperature (RT, 22°C) center shift, relative to the spectrum of a metallic iron foil at RT, verses the RT quadrupole splitting for Fe_{oct} in minerals containing either Fe^{2+} or Fe^{3+} ions. It is clear from figure 4 that the magnitudes of δ and Δ are distinctive for these two valence states of iron. Typical ranges of RT (δ, Δ) values in mm/sec for Fe^{2+}_{oct} are (0.95 to 1.25, 1.5 to 3.1) whereas the values for Fe^{3+}_{oct} are (0.30 to 0.55, 0.40 to 2.0) (Dyar, 1987; Greenwood and Gibb, 1971). The result is that samples such as biotite, which contain octahedrally coordinated iron in both valence states, have RT Mössbauer spectra composed of ion-specific subspectra that can be unambiguously assigned to Fe^{2+}_{oct} and Fe^{3+}_{oct}.

In figure 5 we show a RT spectrum of our single crystal biotite. The positions of the valence-specific subspectra are indicated based upon the characteristic (δ, Δ) values. It follows that the first peak (peak A),

Fig. 4 Center Shift versus Quadrupole Splitting

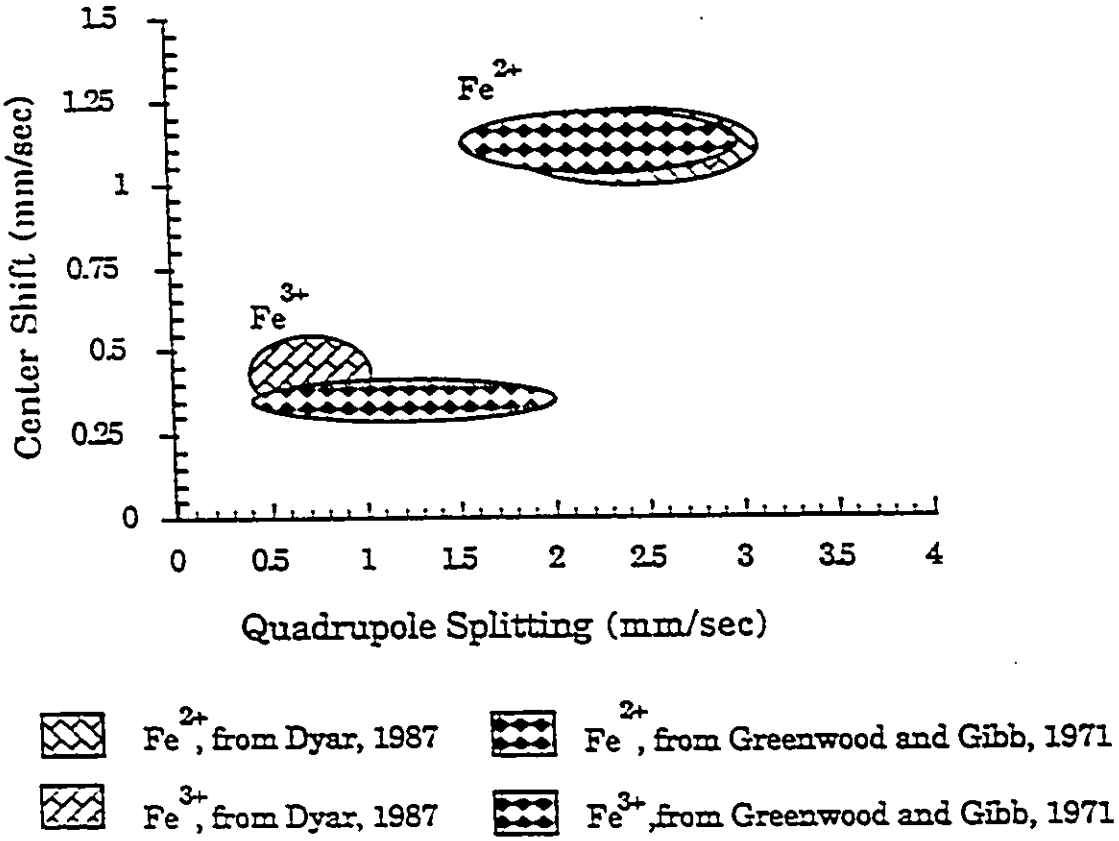

Fig. 4 Center Shift versus Quadrupole Splitting of octahedrally coordinated Fe^{2+} and Fe^{3+} in minerals

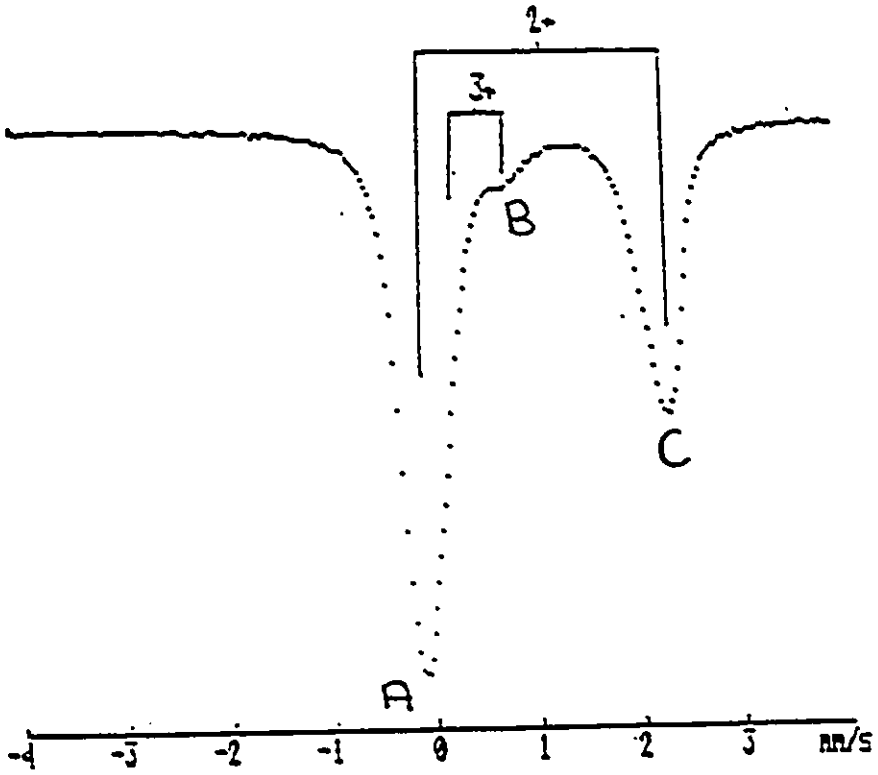

Fig. 5 Typical room temperature spectrum of MOC2661 biotite

The valence-specific suspectra for Fe^{2+} and Fe^{3+} are schematically shown. Peaks A, B and C correspond to the first, second and third peaks in the direction of negative to positive velocity.

centered on ~ - 0.1 mm/s, mainly consists of a combination of low energy lines of quadrupole doublets of Fe^{2+} and Fe^{3+} in octahedral coordination. The shallow peak (peak B), centred on ~ + 0.8 mm/sec, mainly consists of the high energy lines of the quadrupole doublets of Fe^{3+} in octahedral coordination, and the peak centred on ~ +2.3 mm/sec (peak C) consists of the high energy lines of the quadrupole doublets of the octahedrally coordinated Fe^{2+}.

Distinguishing the Fe^{2+} and Fe^{3+} subspectral areas is complicated by the overlapping of their low energy spectral contributions (in peak A). However, this problem can be overcome because the part of the spectral intensity assigned to the low energy line of the Fe^{2+} subspectrum is proportional to the intensity of it's high energy partner (peak C). The proportionality constant is a function of the orientation of the single crystal with respect to the gamma ray radiation direction. All our experiments use the same orientation.

In oxidation work, where, for a sample that is measured in a given orientation, we change the Fe^{2+} and Fe^{3+} amounts, we will want to assume that the ratio, R, of the low to high energy line intensities of a subspectral doublet, remains constant regardless of the relative amounts of Fe^{3+}. Obtaining the Fe^{2+} and Fe^{3+} subspectral areas will then be possible and will rely upon defining the high energy Fe^{2+} contribution (i.e. fitting peak C). The main details concerning these points are given in section 5.2.

3.4 Fitting a single spectrum

Recent developments in the analysis of Mössbauer spectra have shown that a lineshape composed of Voigt, rather than Lorentzian, functions is better suited to model spectral distortions caused by thickness effects (see section 4.4) and the hyperfine parameter distributions (Rancourt, 1989; Rancourt and Ping, 1991). The hyperfine parameter distributions, either of Lorentzian line positions or quadrupole splittings, can be represented by sums of Gaussians. Analytically, this summation produces a lineshape, $N(\psi)$, that is a sum of Voigts. This lineshape gives the number of gamma rays for each channel or gamma ray energy, ψ, and can be expressed as:

$$N(\psi) = BG - \sum_i V(h_i, \gamma_i, \sigma_i, w_i ; \psi) \qquad (17)$$

where BG is the flat background of the spectrum, and the sum is over the Voigt functions used in the particular model, or fit. The Voigt function is defined as:

$$V(\psi) = \int_{-\infty}^{\infty} dz\, G(z) L(\psi - z) \qquad (18)$$

where

$$G(z) = \frac{1}{\sigma \sqrt{2\pi}} \exp\left[\frac{-(z - w)^2}{2\sigma^2}\right] \tag{19}$$

and

$$L(\psi - z) = \frac{h \frac{\gamma^2}{4}}{(\psi - z)^2 + \frac{\gamma^2}{4}}. \tag{20}$$

$L(\psi-z)$ is a Lorentzian function of height h, FWHM γ and centered upon velocity z. The i^{th} Voigt, as a function of energy ψ, is therefore described by a Lorentzian height h_i, a Lorentzian FWHM γ_i, a Gaussian width σ_i, and a center position w_i.

The spectral area assigned to an observed peak can be obtained from the Voigt lines that model that part of the spectrum. The area of the ith Voigt is:

$$A_i = \frac{\pi h_i \gamma_i}{2} \tag{21}$$

Assuming the γ_i is the same for all Voigts used in the model, the ratio of the peak area, A_p, to the total area of the spectrum, A_{total}, is:

$$\frac{A_p}{A_{total}} = \frac{\sum_m A_m}{\sum_i A_i} = \frac{\sum_m h_m}{\sum_i h_i} \qquad (22)$$

where the top sum runs over the Voigt lines in the peak, and the bottom sum runs over all the Voigt lines in the spectrum. Equations (16) and (22) will be used to determine the relative Fe^{2+} subspectral area and, consequently, the Fe^{2+} population.

The choice of a model for a spectrum, or several spectra, depends upon how well the theoretical lineshape can represent the experimental data. In this work, the quality of a particular fitting model is estimated by the value of the chi-squared (χ^2) function, which is given as:

$$\chi^2 = \sum_k \left\{ \frac{[\, N(a_1,\ldots,a_j,\ldots,a_p\,;\,\psi_k) - C_k]}{\sqrt{C_k}} \right\}^2 \qquad (23)$$

where C_k is the number of gamma rays counted in the k^{th} velocity channel and $N(a;\psi_k)$ is the theoretical number of counts in channel k as predicted

using the multidimensional vector a. The experimental error in absorption experiments is given as $\sqrt{C_k}$.

It is common practice to normalise the χ^2 such that we eliminate its dependence on the number of parameters fixed during the fitting process. This standard function is called the reduced chi-squared ($\chi^2_{red.}$) and is defined by:

$$\chi^2_{red.} = \frac{\chi^2}{\nu} \tag{24}$$

where ν is the number of degrees of freedom for the model. In our case, ν is equal to the number of channels of data less the number of free parameters.

A minimum value of χ^2 is found when the values of $N(a; \psi_k)$ and C_k are the closest together in the χ^2 sense. In general, an "acceptable" fit has a $\chi^2_{red.} = 1$ (or $\chi^2 = \nu$), which is based upon the idea that the $\chi^2_{red.}$ is normally distributed about 1 with a standard deviation of $\sqrt{(2/\nu)}$ (Press et al, 1988). Consequently, a model having a $\chi^2_{red.}$ value that is several standard deviations away from 1 implies that the particular model being tested is most probably incorrect.

In our analysis, the model used to obtain robust spectral areas for Fe^{2+} and Fe^{3+} must adequately describe the areas of the observed absorption peaks of a spectrum. While it would be preferable to use a model that is within the Gaussian distribution of the χ^2_{red}, it is possible to find the areas of the observed absorption peaks without having a probably correct model for the data set (see section 5.2).

3.5 Spectral fitting techniques

Two common techniques to fit a group of related spectra are the individual fit and the multifit. Traditionally, areas of observed peaks have been obtained from good quality fits of a model to single spectra (individual fits). Multifits can also be used in which some of the fitting parameters are constrained to be the same for all spectra in a given group of spectra. This technique takes advantage of expected common spectral features.

Individually fitting each spectrum means that the set of $(h_i, \gamma_i, \sigma_i, w_i)$ parameters, used to describe the i^{th} Voigt line in a model, are optimized such that the model attempts to give the best possible lineshape for each particular spectrum. However, to apply equation (22), the parameter γ_i must be constrained to be the same for all Voigt lines used to model a single spectrum. This constraint suggests that the elemental lines that make up a spectrum have similar Lorentzian FWHM. If the resulting lineshape satisfactorily represents an observed peak then the Voigt line parameters that describe the observed peak may be used to extract the observed peak's spectral area.

Simultaneously fitting, or multifitting, a group of spectra is an alternative way to find spectral areas of the observed peaks. In our

multifits, a group of spectra have a common (i.e. constrained to be the same for each spectrum in the group but variable) set of $(\gamma_i, \sigma_i, w_i)$ parameters that describe the i^{th} Voigt line in a model. In fact, the Lorentzian FWHM's (γ_i) are also constrained to be the same for each Voigt line in each spectrum ($\gamma_i = \gamma$, for each i and for each spectrum in a group). This means that the background (BG) and the heights of the Voigt lines are free parameters that can be individually adjusted to optimize the lineshape for each spectrum. In this manner, the spectrum's optimized height parameters may be used to determine the amounts of Fe^{2+} and Fe^{3+} (see section 5.2).

For convenience, an A-B-C fitting notation will be used to describe our fitting models. For a particular model of a spectrum (or set of spectra), the number of Voigt lines used to fit each observed peak replaces the corresponding letter. For example, the lineshape of a 1-2-3 model consists of a single Voigt line in peak A, two Voigt lines in peak B and three Voigt lines in peak C. If an A-B-C model is fitted using the individual fitting technique, then the model is denoted as an A-B-C/I fit, whereas a multifit of the model is referred to as an A-B-C/M fit..

4. Sample Characterization and Experimental Arrangement

4.1 Characterization of MOC2661 biotite

Our absorbers were cleaved from a 4cm x 5cm x 1cm single crystal six-sided slab of biotite found in the region of the Silver Crater mine near Bancroft, Ontario. We obtained this sample, labelled as MOC2661, from the Canadian Museum of Nature, Mineral Sciences division.

The sample's chemical composition was determined by Dr. A.E. Lalonde using wavelength dispersive X-ray spectrometry with the Camebax electron microprobe from the McGill University Microprobe Laboratory. Table 1 lists the minimum, maximum and mean values from three determinations for the 11 elements analyzed. The total amount of iron is quoted as FeO (Fe^{2+}) since the electron microprobe cannot distinguish the valence states of iron. Four spot analyses, across a 4cm x 2cm single crystal wafer of MOC2661 biotite using a beam with a diameter of 5μm, showed constant chemical composition for all the component oxides that are listed in table 1.

The structural formula unit shown in table 2 is calculated using an imposed tetrahedral site occupancy of 8 and an anion content of 24. Twenty of these anion sites were assigned to oxygen. Since it is possible to

Table 1 Chemical Analysis of MOC2661 biotite

	minimum (wt.%)	maximum (wt.%)	mean[a] (wt.%)
SiO_2	38.28	38.54	38.42
TiO_2	2.00	2.36	2.22
Al_2O_3	11.01	11.23	11.12
FeO[b]	17.75	18.48	18.12
MnO	0.85	0.95	0.90
MgO	13.48	13.77	13.67
Na_2O	0.51	0.56	0.54
K_2O	9.47	9.59	9.54
H_2O			1.85[c]
F	3.54	4.61	4.23
Cl	0.06	0.10	0.08
O=F			-1.78[d]
O=Cl			-0.02[d]
Total			98.89

[a]. Minimum, maximum, and mean values of three analysis.
[b]. All iron content expressed as FeO.
[c]. Water content calculated as explained in the text.
[d]. Equivalent oxygen weight corrected for F and Cl.

Table 2 Structural formula based on 20 oxygens

Tetrahedral sites	Si^{4+}	5.92
$\sum = 8.00$[a)]	Al^{3+}	2.02
	Ti^{4+}	0.06
Octahedral sites		
$\sum = 5.79$	Mg^{2+}	3.14
	Fe^{2+}	2.34
	Ti^{4+}	0.20
	Mn^{2+}	0.12
Interlayer sites		
$\sum = 2.04$	K^{+}	1.88
	Na^{+}	0.16
Anions		
$\sum = 24.00$[b)]	O^{2-}	20.00
	F^{-}	2.06
	OH^{-}	1.92
	Cl^{-}	0.02

a). A tetrahedral site occupancy of 8 was imposed.

b). We imposed an oxygen occupancy of 20 and a calculated OH^{-} amount such that $OH^{-} + F^{-} + Cl^{-} = 4$, giving a total anion stoichiometry of 24.

substitute either fluorine (F^-) or chlorine (Cl^-) for the hydroxyl group, the combined occupancy of (OH^-, F^-, Cl^-) was restricted to 4.

The sample is a true trioctahedral biotite having an Fe/(Fe+Mg)=.43, and a negligible divalent interlayer cation content. Based on the imposed tetrahedral site occupancy and restricted anion content, the total octahedral and interlayer site occupancies were calculated at 5.78 and 2.04 per structural formula unit, respectively. These structural formula calculations were also performed by Dr. A.E. Lalonde of the Geology Department at the University of Ottawa.

Finally, it is worth noting that Fe^{3+} can sometimes occupy the terahedral sites in biotite. Recently, however, Rancourt et al. (1992) have shown that this leads to a distinctive feature in the Mössbauer spectra. Since the spectra of MOC2661 do not contain this feature, we must conclude that there is no tetrahedral iron in our biotite.

4.2 Equipment

In our experiments, room temperature (22°C) ^{57}Fe transmission Mössbauer spectra were collected using a 10mCi ^{57}Co source in a rhodium matrix. During the decay process of ^{57}Co, ^{57}Fe nuclei in the first excited state can be produced. These ^{57}Fe nuclei de-excite to produce the 14.4 keV gamma rays that may be absorbed by the ^{57}Fe nuclei in our biotite sample.

To impart the required Doppler shift to the emitted gamma rays, the source was placed on a Mössbauer transducer. The transducer operated in constant acceleration mode covering a $\pm$ 4 mm/sec velocity range.

A small hole in the lead shielding surrounding the transducer permits radiation to reach the absorbing material. The number of gamma rays that pass through the absorber are counted, and stored in a memory channel that is associated with a particular transducer velocity.

4.3 Data acquisition

In our experiments, radiation is detected by a proportional counter that generates a signal proportional to the gamma ray energy. This signal is first amplified and then filtered by a single channel analyzer (SCA) such that only pulses of approximately 14.4 keV energy are passed to the channel memory.

A time-based electronic system ensures that the data accumulated in a particular channel corresponds to a particular gamma ray energy or transducer velocity. If the maximum channel number of 1024 is passed, the detected counts are ignored until a synchronizing pulse starts a new cycle of memory loading, in step with the transducer motion.

Using this Mössbauer apparatus, we can acquire two 512-channel spectra during one Mössbauer experiment. These spectra are approximately mirror images of each other; one spectrum corresponding to increasing energy, the other to decreasing energy.

These spectra must be "folded" to obtain a flat background level and calibrated to obtain the precise energy (or velocity) scale. We used room temperature spectra of an ^{57}Fe enriched foil, collected prior to and following each Mössbauer experiment, for calibration. Details concerning the folding and calibration processes can be found in M. Royer M.Sc. thesis, 1991.

4. 4 Absorber preparation and absorber thickness effects

Our biotite specimens were fragile and required special care. To avoid losing sample mass during handling, each specimen was sandwiched between two layers of acetate and the sample was centred on a 1/2 inch diameter window in an aluminum holder. This absorber assembly was taped to the spectrometer housing such that the sample's cleavage plane was perpendicular to the direction of incident gamma radiation. All Mössbauer experiments were performed with the source and absorber at room temperature (22^0 C).

Experimental problems arising from the thickness of the absorber can cause line broadening of the observed peaks. This is related to the gamma ray flux at different depths in the absorber. Gamma rays incident on the absorber are scattered and/or absorbed. This means absorbing nuclei at greater depths of the absorber will see a reduced gamma ray flux at the resonance frequencies and therefore, have fewer absorptions. The thickness of the absorber can therefore cause an attenuation of the absorption peaks. This attenuation is more noticeable in deeper absorption peaks.

Fortunately, there exists a method to estimate the degree of attenuation of an observed absorption peak for a given physical thickness of the absorber. The effective absorber thickness can be defined as:

$$t_a = f_a n_a \sigma_o \quad (25)$$

where t_a is the thickness parameter, f_a is the absorber recoil free fraction, n_a is the number of ^{57}Fe nuclei per unit area of the absorber, and σ_o is the resonance cross-section for the 14.4 keV Mössbauer transition. A graphical relationship has been established between t_a and an absorber correction factor, A/A_{th}, for various minerals (Rancourt et al., 1992). Once the area (A) of an observed peak is determined from fitting, and t_a is evaluated from the absorber's physical parameters, the thickness corrected area (A_{th}) can be found. Essentially, A_{th} is the spectral area of an observed peak that would have been produced if the gamma ray flux had been uniform throughout the depth of the absorber.

In our case, the thickness correction factors were used to find the thickness corrected ratio of the area of an observed peak to the total area of a spectrum. The thickness correction factor for the total spectral area is the weighted sum of the correction factors for peaks A, B, and C. The weighting factor for observed peak p is A_p/A_{total}. The correction factors for both the individual peaks and the total spectrum were found to be ~1 such that thickness corrections were not considered necessary for our work.

4.5 Annealing temperature

Since the sample's annealing temperature is an important consideration in this work, several factors were considered in order to estimate the sample's temperature uncertainty. The absolute temperature error with our Pt/Rh thermocouple arrangement was $\leq 1^{\circ}$ C, as checked by an ice water measurement. Since some samples were exposed for long periods of time, the temperature stability of the furnace was also checked, and a variation of $\pm 6^{\circ}$ C was observed. The spatial temperature non-uniformity across the single crystal sample was approximately $\pm 3^{\circ}$ C. Taking the above factors into consideration, we have a total uncertainty of less than $\pm 10^{\circ}$ C.

5. Experimental Results and Interpretation

5.1 Measured Mössbauer spectra

To examine the time and temperature dependence of the oxidation of Fe^{2+} in our biotite sample, we have collected two series of spectra that are classified in terms of the annealing time and temperature.

In order to study the time dependence of iron oxidation in our sample, each RT spectrum of the "time series" was collected after annealing in air at 732^0 C for some total time.

The "temperature series" also consists of several spectra. In this case each RT spectrum was collected after annealing in air for 24 hours at a specified temperature between 426^0 C and 875^0 C.

The temperature series spectra are shown in figure 6. The effect of oxidation is obvious: more and more of the original Fe^{2+} becomes Fe^{3+} as the annealing temperature is increased. Time, at a given temperature, has an analogous effect (see figure 10).

Fig. 6 RT Mössbauer spectra for the Temperature series.
Room temperature Mossbauer spectra of MOC2661 biotite, each sample has been annealed in air for 24 hours at the indicated temperatures. The * indicates that the sample has been heated for 94 instead of 24 hours.

Fig. 6 RT Mössbauer spectra for the temperature series

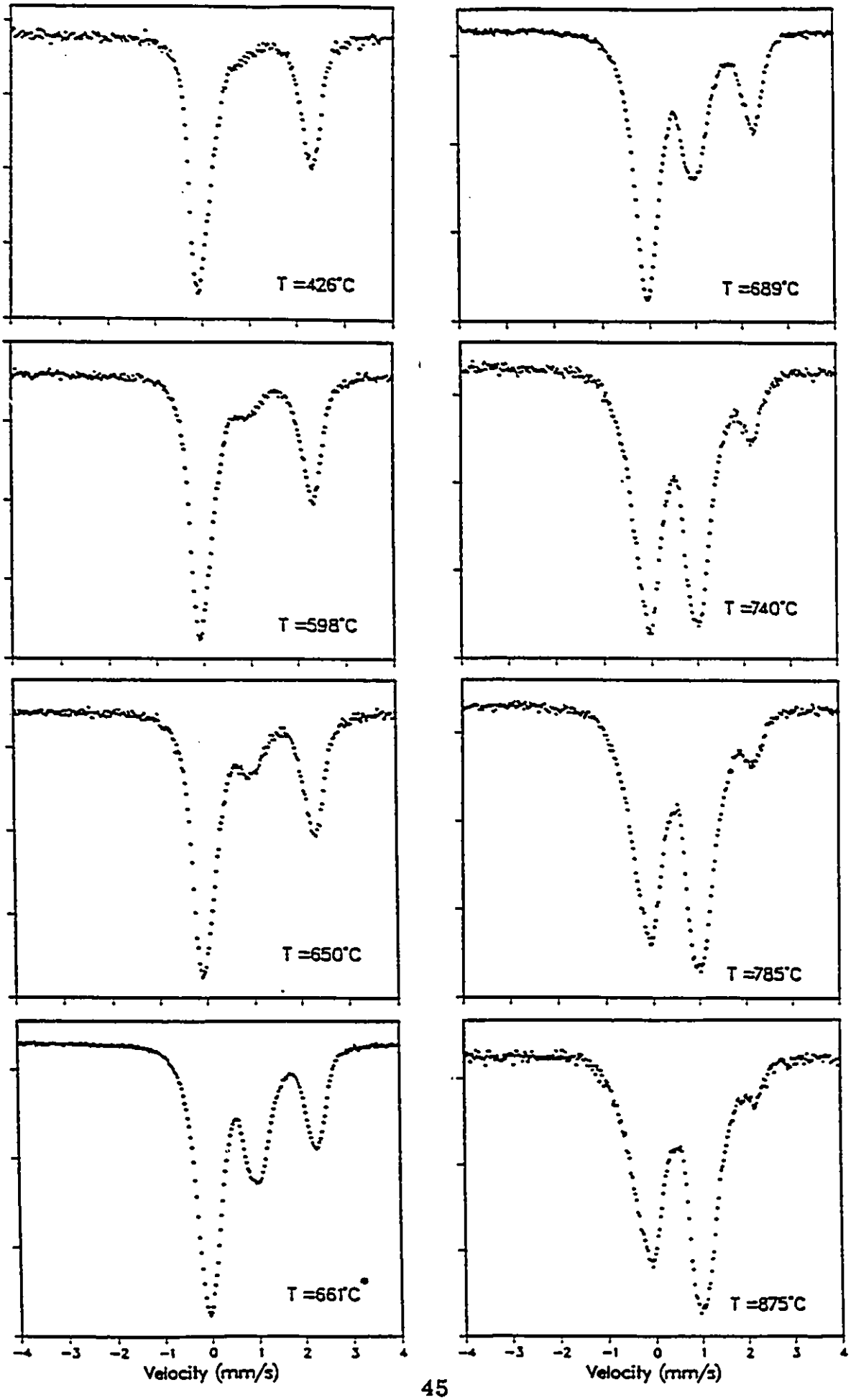

5.2 Comparison of spectral features and some preliminary implications

Before we quantify the relative amounts of Fe^{2+} and Fe^{3+}, it is useful to have a general description of how the intensities of the observed peaks vary in the spectra of our oxidized biotite. At low annealing temperatures (or short exposure times), most of the spectral intensity is located in peaks A and C. Peak A is the dominant peak and is centered around ~ -0.1 mm/sec, while peak C is a well resolved peak centered around +2.3 mm/sec (see figures 5 and 6). At this degree of Fe^{2+} oxidation, peak B is quite small and appears to be centered around +0.8 mm/sec.

In comparison, the spectra of more oxidized biotite samples (i.e. the samples that have been annealed at higher temperatures or for longer exposure times) have most of their intensity in peaks A and B. It appears that peak A has lost some relative depth and has developed a pronounced shoulder around the -0.8 mm/sec region, while peak B has developed into a broad, deep and asymmetric peak that is centered about ~ +1.0 mm/sec. At the same time that the changes in peaks A and B occur, peak C also loses some intensity, especially on its high velocity side.

The progressive changes in the shapes of the observed peaks, in either the time or temperature series, suggest that there is a preferential oxidation of Fe^{2+} ions in certain crystallographic sites. By inspection, the

gradually diminishing intensity on the positive velocity side of peak C (recall peak C represents the high-energy lines of the Fe^{2+} subspectral doublets) coincides with the growth of peak B (the high-energy lines of the Fe^{3+} subspectral doublets). This indicates that elemental doublets arising from Fe^{2+} ions in a group of crystallographic sites that have large quadrupole splittings (Δ's) are disappearing first to become Fe^{3+} elemental doublets. This shows that certain Fe^{2+} (in octahedral sites with large Δ's) oxidize more readily than other Fe^{2+} ions (in octahedral sites with smaller Δ's). These points are illustrated in figures 7a and 7b where we show a plot of rescaled fitted total lineshapes in the regions of peaks B and C for the temperature series spectra. While such observations are very interesting, they are not the main focus of the present thesis, we are only concerned with evaluating total Fe^{2+} and Fe^{3+} populations.

Near the biotite decomposition temperature, ~ 900^0 C, essentially all of the Fe^{2+} is expected to have been converted into Fe^{3+}. This would have produced a spectrum with intensity at the locations of peaks A and B (Hogg and Meads, 1975). This expected result does not agree with the finite Fe^{2+} contribution seen at the location of peak C in our 875^0 C spectrum. Our results suggest that a certain population of Fe^{2+} is very resistant to oxidation and that these Fe^{2+} may persist up to structural breakdown of the biotite lattice.

Fig 7a Rescaled fitted intensity of peak B versus velocity for the Temperature series spectra

Notice that an increase in sample annealing temperature is associated with an increase in intensity on the high velocity side of peak B. Correspondingly, this peak becomes centered on a slightly higher velocity. Each curve is for a particular temperature:

curve 1 = 426^0 C, curve 2 = 598^0 C, curve 3=650^0 C, curve 4 = 661^0 C

curve 5 = 698^0 C, curve 6 = 740^0 C, curve 7=785^0 C, curve 8 = 875^0 C.

Fig 7a

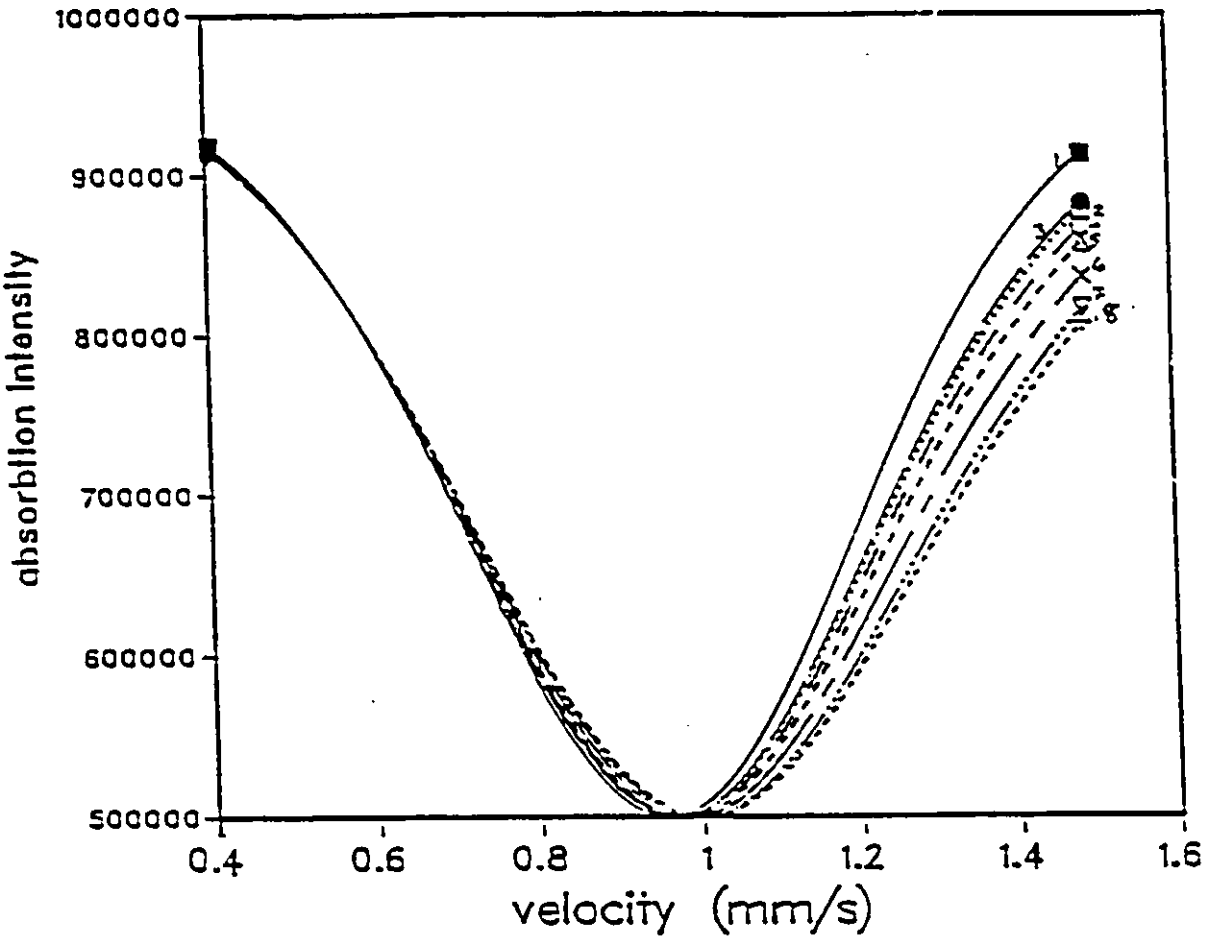

Legend

■ CURVE 1 ● CURVE 3 △ CURVE 5 ▽ CURVE 7

□ CURVE 2 ○ CURVE 4 × CURVE 6 + CURVE 8

Fig 7b Rescaled fitted intensity of peak C versus velocity for the Temperature series spectra

Notice that an increase in sample annealing temperature is associated with a decrease in intensity on the high velocity side of peak C. Correspondingly, this peak becomes centered on a lower velocity. Each curve is for a particular temperature:

curve 1 = 426^0 C, curve 2 = 598^0 C, curve 3 = 650^0 C, curve 4 = 661^0 C, curve 5 = 698^0 C, curve 6 = 740^0 C, curve 7 = 785^0 C, curve 8 = 875^0 C.

Fig7b

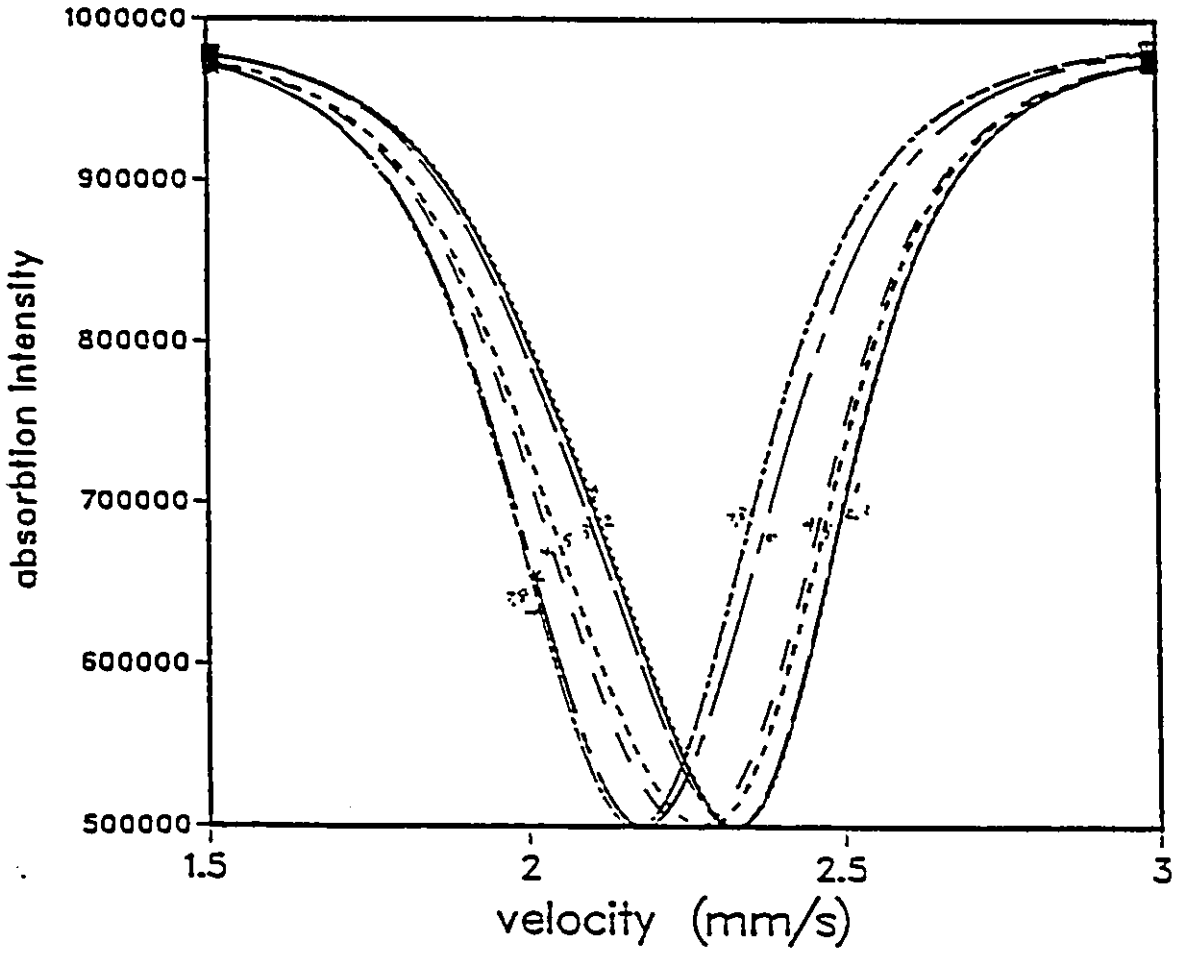

Legend

■ CURVE 1 ● CURVE 3 △ CURVE 5 ▽ CURVE 7

□ CURVE 2 ○ CURVE 4 × CURVE 6 + CURVE 8

5.2 Calculation of the relative amounts of Fe^{2+} and Fe^{3+} from various fitting models

The relative amounts of Fe^{2+} and Fe^{3+}, that is Fe^{2+}/Fe_{total} and Fe^{3+}/Fe_{total} respectively, may be found from our spectra by using the following relationship:

$$\frac{Fe^{2+}}{Fe_{total}} = \frac{A_{2+}}{A_{total}} = \frac{H_{2+} + L_{2+}}{A_{total}} \qquad (26)$$

where H_{2+} and L_{2+} are the areas of the high and low energy lines of the Fe^{2+} subspectrum, respectively, and A_{total} is the total spectral area. H_{2+} is the area of the observed peak C and L_{2+} is a fraction of the area of peak A. The remaining spectral area (A_{total} - A_{2+}) can be assigned to the Fe^{3+} subspectrum.

To obtain reliable observed peak areas and to estimate the uncertainty in these areas, our spectra have been both individually and multifitted using several different models. Single spectra were individually fitted using a nonlinear least squares fitting IBM/PC program developed by Dr. J. Ping and Dr. D. Rancourt. The multifitted spectra used the nonlinear least squares fitting program MINUIT, which was developed at the Centre européen pour la recherche nucléaire (James and Roos, 1975). Using both of these fitting techniques for our various models enabled us to find a

dependable average spectral area for each peak in each spectrum. To illustrate the quality of some of these fits, a selection of the various models and their resulting spectral lineshapes are presented in the following figures.

The easiest way to estimate if a model has successfully represented an observed peak is to visually examine the spectral lineshapes. For example, fitting the spectra using a model with a single Voigt line in each absorption peak (1-1-1 fits) demonstrated that peaks A and C are asymmetric about their respective minima in most of the spectra (see figure 8 for a 1-1-1/M of the temperature series). This indicates that at least two Voigt lines may be required in order to model the asymmetry of both peaks A and C. An example of 2-1-2/M lineshapes for the temperature and time series can be found in figures 9 and 10, respectively. Various other models, such as 2-2-2 fits, were also evaluated to ensure that all the peaks in all the spectra are well represented. The resulting parameters of all the different fitting models are listed in appendix A.

The average area assigned to an observed peak (p) has been found in terms of the fraction h_p/h_{total}, where h_p is the sum of the Lorentzian heights of the Voigt lines used to fit observed peak p and h_{total} is the sum of the Lorentzian heights of all the Voigt lines used in the spectrum. Tables 3, 4, and 5 list the results h_A/h_{total}, h_B/h_{total}, and h_C/h_{total}, for the temperature series spectra.

Fig8 1-1-1 Multifit of the Temperature series spectra

In each spectrum the solid points represent the data and the solid line through the points is the theoretical lineshape. The corresponding fit parameters are given in table A4 of the appendix. The * indicates that this sample has been heated for 94 instead of 24 hours.

Fig 8 1-1-1 Multifit of the Temperature series spectra

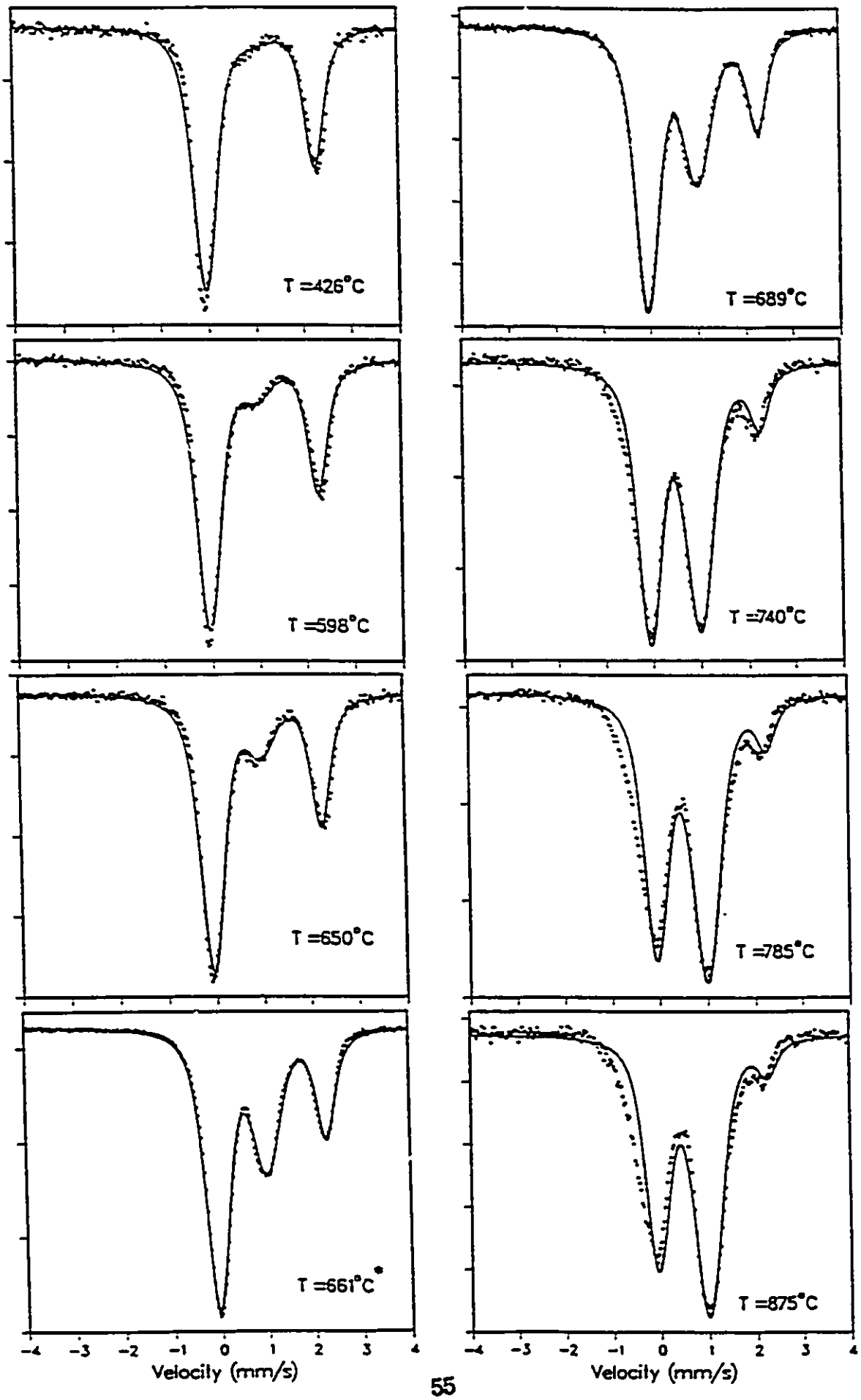

Fig9 2-1-2 Multifit of the Temperature series spectra

In each spectrum the solid points represent the data and the solid line through the points is the theoretical lineshape. The corresponding fit parameters are given in table A5 of the appendix.

Fig 9 2-1-2 Multifit of the Temperature series spectra

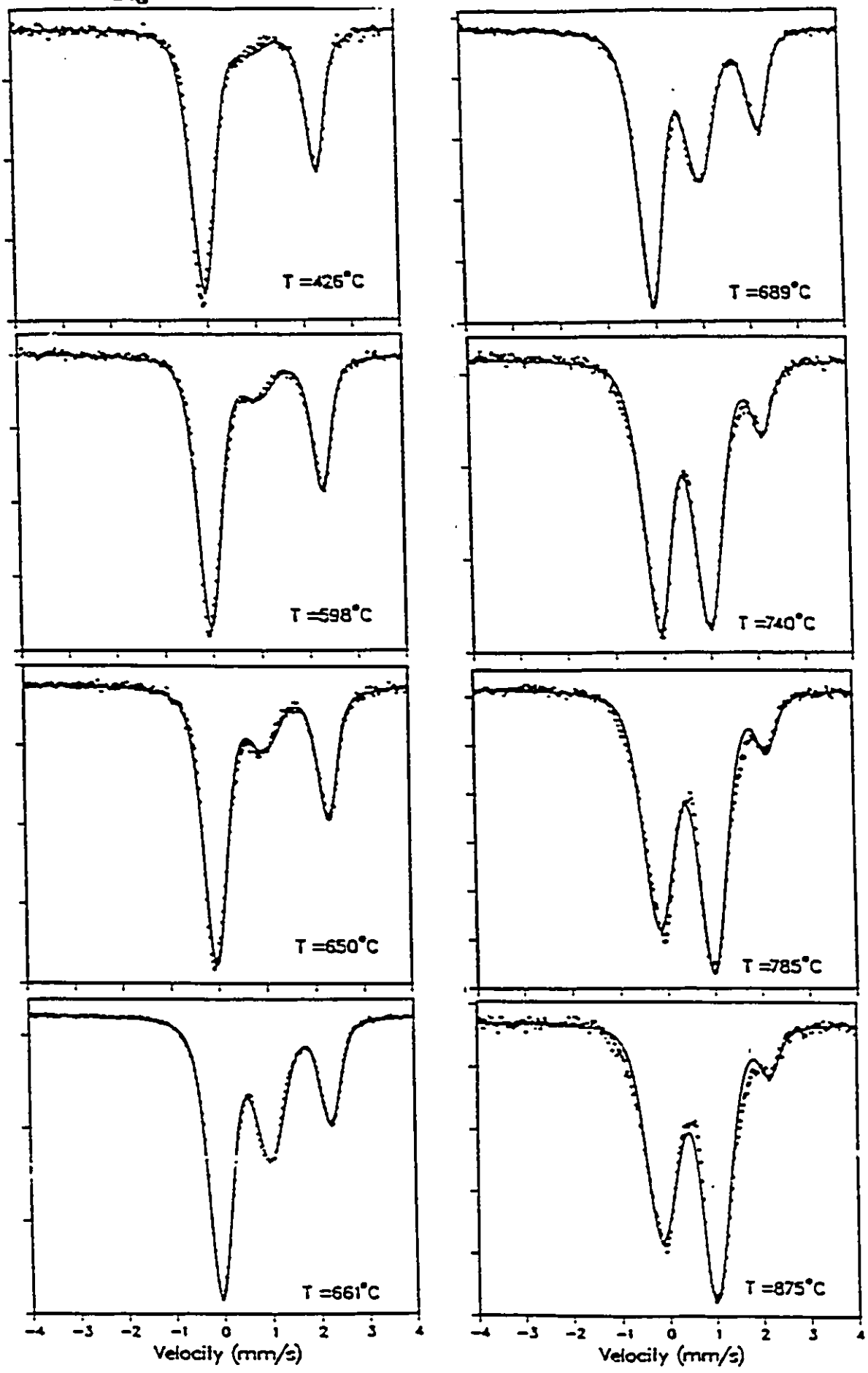

Fig10 2-1-2 Multifit of the Time series spectra

In each spectrum the solid points represent the data and the solid line through the points is the theoretical lineshape. The corresponding fit parameters are given in table A14 of the appendix.

Fig 10 2-1-2 Multifit of the Time series spectra

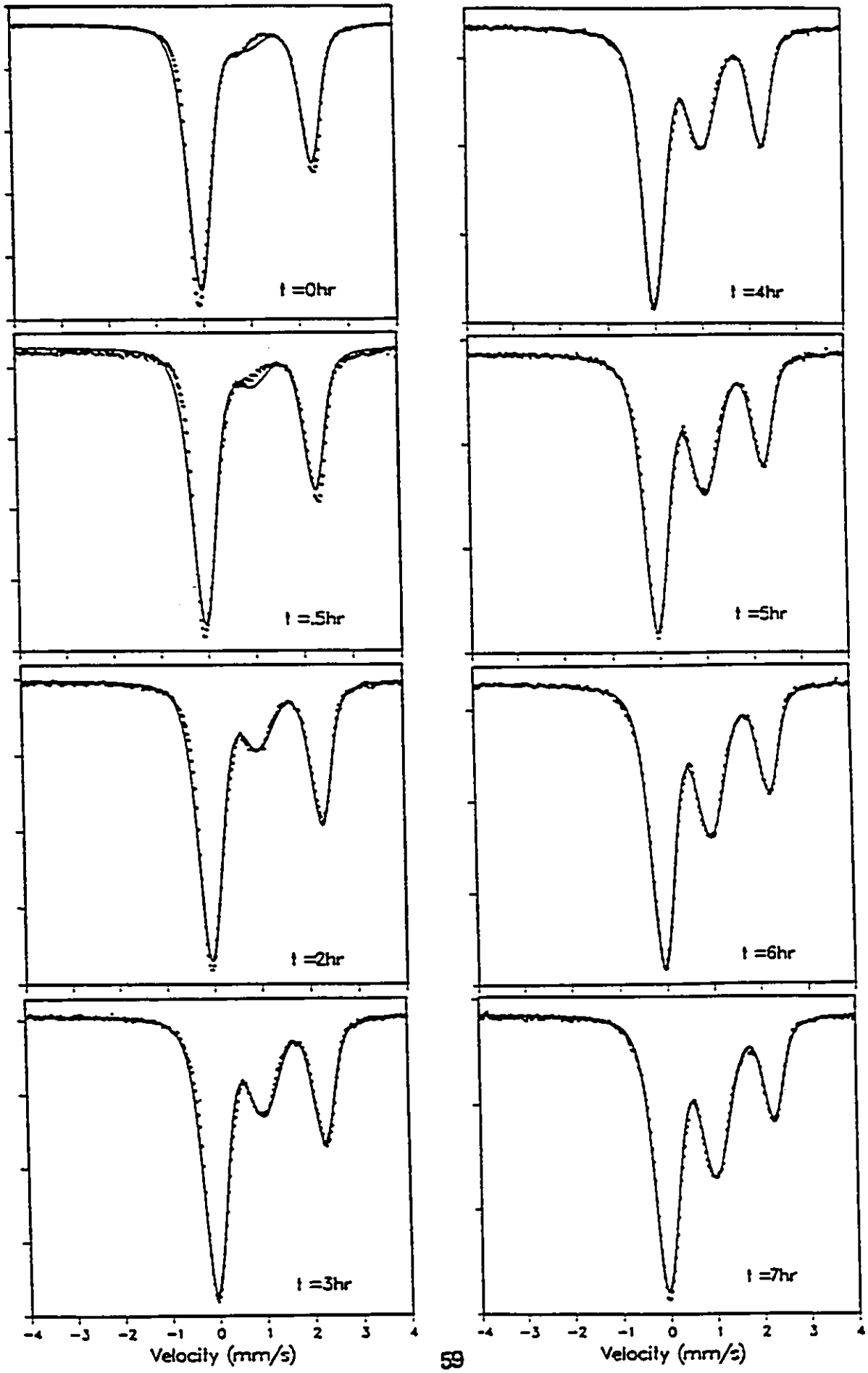

Fig 10 continued

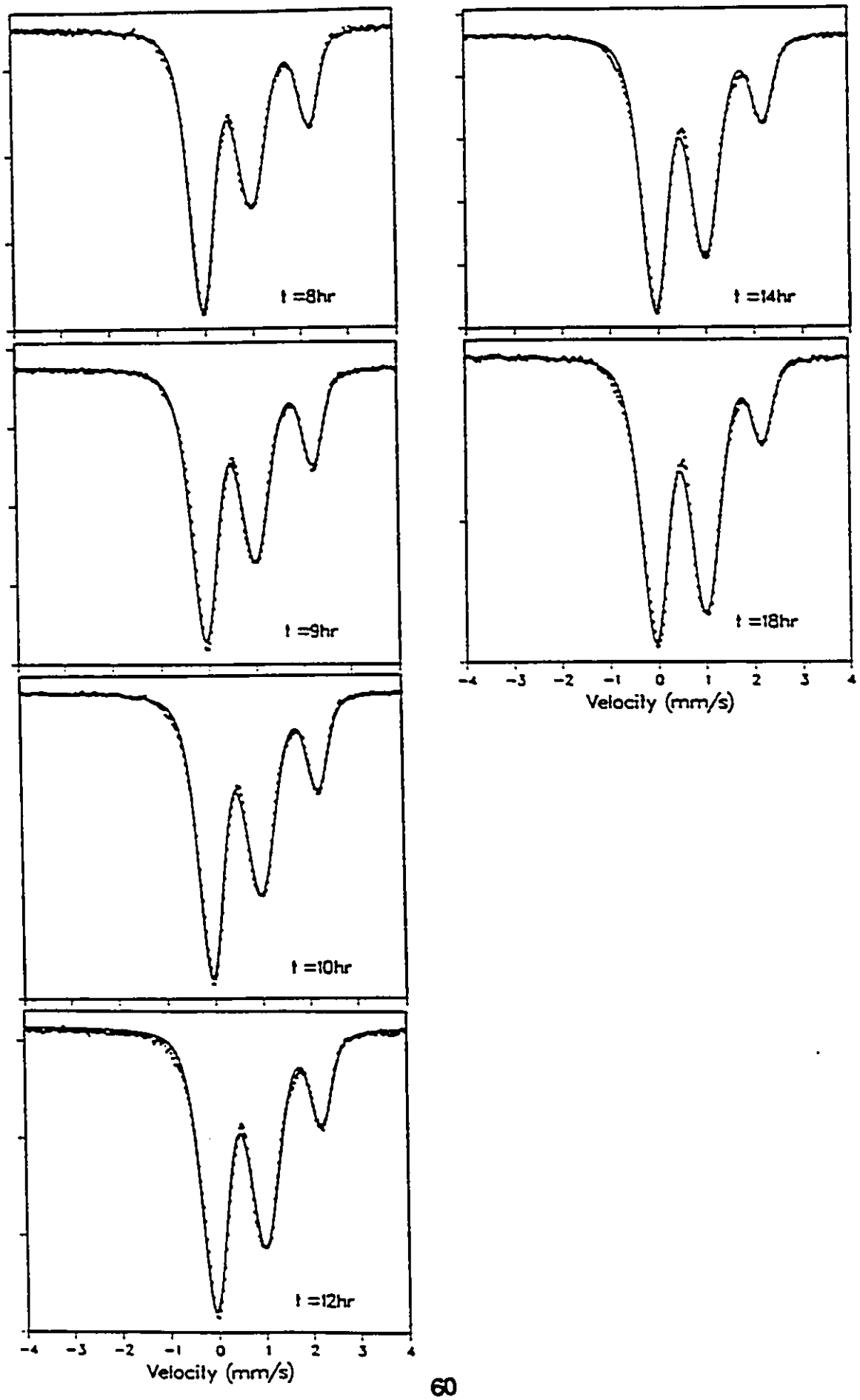

Table 3

h_A/h_{total} from Individual and Multifits of the Temperature Series[a)]

Fit/type[b)]	426	598	650	661	689	740	785	875
1-1-1/M	.673	.650	.620	.537	.530	.448	.423*	.405*
2-1-2/M	.657	.637	.607	.527	.524	.454	.443	.429
2-2-1/M	.663	.641	.612	.527	.526	.452	.437	.423
2-2-2/M	.661	.640	.612	.530	.528	.460	.447	.435
3-2-2/M	.660	.638	.608	.533	.536	.464	.446	.428
1-1-1/I	.598*	.545*	.565*	.534	.527	.462	.444	.434*
2-2-1/I	.664	.623	.598	.543	.541	.459	.452	.442
mean	.663	.638	.610	.533	.531	.457	.445	.431
s.d.[c)]	±.005	±.009	±.007	±.006	±.006	±.006	±.005	±.007

a. Temperature ± 10°C

b. M = Multifit, I = Individual.

c. s.d. = standard deviation

*. Incorrect due to unphysical line positions and widths. These values were not included in the calculations of the mean values or of the standard deviations.

Table 4

h_B/h_{total} from Individual and Multifits of the Temperature Series[a)]

Fit/type[b)]	426	598	650	661	689	740	785	875
1-1-1/M	.022	.079	.129	.288	.307	.469	.510	.543*
2-1-2/M	.050	.100	.146	.299	.314	.457	.485	.509
2-2-1/M	.036	.092	.142	.306	.322	.481	.522	.546*
2-2-2/M	.049	.096	.143	.296	.312	.457	.490	.515
3-2-2/M	.039	.097	.145	.294	.306	.455	.495	.523
1-1-1/I	.112*	.194*	.190*	.289	.308	.454	.490	.473*
2-2-1/I	.035	.122*	.116	.280	.294	.492	.487	.488*
mean	.039	.093	.137	.293	.309	.466	.497	.516
s.d.[c)]	±.010	±.008	±.012	±.007	±.009	±.014	±.014	±.007

a. Temperature ± 10°C

b. M = Multifit, I = Individual.

c. s.d. = standard deviation

*. Incorrect due to unphysical line positions and widths. These values were not included in the calculations of the mean values or of the standard deviations.

Table 5

h_C/h_{total} from Individual and Multifits of the Temperature Series[a)]

Fit/type[b)]	426	598	650	661	689	740	785	875
1-1-1/M	.305	.271	.250	.175	.163	.083	.067*	.053*
2-1-2/M	.293	.263	.246	.175	.163	.088	.072	.063
2-2-1/M	.300	.268	.246	.168	.153	.067*	.041*	.030*
2-2-2/M	.297	.264	.245	.176	.161	.082	.063	.051
3-2-2/M	.301	.266	.247	.174	.159	.081	.059	.049
1-1-1/I	.307	.261	.245	.176	.165	.085	.066	.093*
2-2-1/I	.300	.255	.249	.177	.165	.049	.061	.070*
mean	.300	.264	.247	.174	.161	.078	.064	.054
s.d.[c)]	±.005	±.005	±.002	±.003	±.004	±.014	±.005	±.008

a.Temperature ± 10°C

b. M = Multifit, I = Individual.

c. s.d. = standard deviation

*. Incorrect due to unphysical line positions and widths. These values were not included in the calculations of the mean values or of the standard deviations.

Similarly, h_A/h_{total}, h_B/h_{total}, and h_C/h_{total} are listed in tables 6, 7, and 8 for the time series spectra. Observed peak areas that appeared to be incorrectly modelled (i.e. misfit) were not included in the mean areas of the observed peaks.

Our next task is to determine the fraction of the area of peak A that corresponds to L_{2+}. This problem can be approached by using the assumption that the ratio, R, of the low to high energy line intensities of an ion-specific subspectral doublet remains constant in all our spectra. That is:

$$L_{2+} = R_{2+} H_{2+} \tag{27}$$

$$L_{3+} = R_{3+} H_{3+} \tag{28}$$

where L_{3+}, and H_{3+} are the low and high energy lines of the Fe^{3+} subspectrum. Therefore,

$$R_{2+} = \frac{A_A - R_{3+}H_{3+}}{H_{2+}} \tag{29}$$

and

$$R_{3+} = \frac{A_A - R_{2+}H_{2+}}{H_{3+}} \tag{30}$$

where A_A and H_{3+} are the spectral areas of peaks A and B, respectively. The values of R_{2+} and R_{3+} have been obtained using the peak areas for the t=0 hour and T = 875°C spectra. The particular peak areas used were those that resulted from the fits to these spectra that were judged to give the most

Table 6

h_A/h_{total} from Multifits of the Time Series[a)]

	0	.5	2	3	4	5	6	7
1-1-1/M	.658	.655	.602	.566	.543	.529	.517	.512
2-1-2/M	.657	.640*	.594	.562	.539	.528	.517	.513
2-2-2/M	.652	.645	.596	.566	.546	.537	.527	.524
3-2-2/M	.655	.653	.612	.572	.524	.542	.514	.525
mean	.656	.651	.601	.567	.538	.534	.519	.519
s.d.[b)]	±.003	±.005	±.008	±.004	±.010	±.007	±.006	±.007

a.Time is in hours

b. s.d. = standard deviation

*. Incorrect due to unphysical line positions and widths. These values were not included in the calculations of the mean values or of the standard deviations.

Table 6 continued...

h_A/h_{total} from Multifits of the Time Series[a)]

	8	9	10	12	14	18
1-1-1/M	.499	.481	.481	.470	.462*	.449*
2-1-2/M	.502	.492	.485	.475	.469	.460
2-2-2/M	.515	.498	.499	.492	.489	.478*
3-2-2/M	.500	.495	.487	.484	.479	.461
mean	.504	.492	.488	.481	.479	.461
s.d.[b)]	±.007	±.007	±.008	±.010	±.010	±.001

a.Time is in hours

b. s.d. = standard deviation

*. Incorrect due to unphysical line positions and widths. These values were not included in the calculations of the mean values or of the standard deviations.

Table 7

h_p/h_{total} from Multifits of the Time Series[a)]

	0	.5	2	3	4	5	6	7
1-1-1/M	.033	.043	.145	.210	.258	.290	.312	.328
2-1-2/M	.053•	.079•	.146	.216	.259	.290	.310	.325
2-2-2/M	.044	.052	.149	.210	.254	.281	.303	.315
3-2-2/M	.033	.039	.134	.200	.254	.279	.314	.318
mean	.037	.045	.144	.209	.256	.285	.310	.322
s.d.[b)]	±.006	±.007	±.007	±.007	±.003	±.006	±.005	±.006

a.Time is in hours

b. s.d. = standard deviation

•. Incorrect due to unphysical line positions and widths. These values were not included in the calculations of the mean values or of the standard deviations.

Table 7 continued...

h_B/h_{total} from Multifits of the Time Series[a)]

	8	9	10	12	14	18
1-1-1/M	.357	.378	.384	.406	.419	.452
2-1-2/M	.350	.365	.376	.392	.410	.435
2-2-2/M	.342	.357	.365	.382	.395	.423*
3-2-2/M	.356	.369	.380	.400	.405	.445
mean	.351	.367	.376	.395	.407	.444
s.d.[b)]	±.007	±.009	±.008	±.010	±.010	±.009

a.Time is in hours

b. s.d. = standard deviation

*. Incorrect due to unphysical line positions and widths. These values were not included in the calculations of the mean values or of the standard deviations.

Table 8

h_C/h_{total} from Multifits of the Time Series[a)]

	0	.5	2	3	4	5	6	7
1-1-1/M	.310	.302	.253	.224	.200	.181	.171	.160
2-1-2/M	.290	.281•	.260	.222	.203	.182	.174	.162
2-2-2/M	.305	.293	.255	.225	.200	.181	.170	.160
3-2-2/M	.312	.309	.256	.228	.202	.180	.173	.158
mean	.304	.301	.256	.225	.201	.181	.172	.160
s.d.[b)]	±.010	±.008	±.003	±.003	±.002	±.001	±.002	±.001

a.Time is in hours

b. s.d. = standard deviation

•. Incorrect due to unphysical line positions and widths. These values were not included in the calculations of the mean values or of the standard deviations.

Table 8 continued...

h_c/h_{total} from Multifits of the Time Series[a)]

	8	9	10	12	14	18
1-1-1/M	.145	.144	.135	.124*	.119*	.100*
2-1-2/M	.149	.143	.139	.133	.121	.106
2-2-2/M	.145	.145	.136	.125*	.115	.101
3-2-2/M	.145	.136	.132	.117	.116	.093
mean	.146	.142	.136	.125	.117	.100
s.d.[b)]	±.002	±.005	±.003	±.011	±.003	±.007

a. Time is in hours

b. s.d. = standard deviation

*. Incorrect due to unphysical line positions and widths. These values were not included in the calculations of the mean values or of the standard deviations.

correct values of the required peak areas (see page A20 of the Appendix). The self-consistent evaluation of R_{2+} and R_{3+} using these areas was achieved as follows. An initial value of R_{2+} was found by assuming $R_{3+}=0$ for the t=0hr spectral areas. Next, an initial value of R_{3+} was determined by using the initial value of R_{2+} and the relevant spectral areas from the 875° C spectrum. Repeated substitution of improved R_{2+} and R_{3+} values into equations (29) and (30) converged to give $R_{2+}=1.981$ and $R_{3+}=0.623$.

Using R_{2+} and equations (26) and (27), the Fe^{2+} subspectral area may be given as:

$$\frac{A_{2+}}{A_{total}} = \frac{h_C\ (\ 1\ +\ R_{2+}\ )}{h_{total}} \qquad (31)$$

we also have:

$$\frac{A_{3+}}{A_{total}} = 1 - \frac{A_{2+}}{A_{total}}, \qquad (32)$$

and, since:

$$\frac{A_{3+}}{A_{total}} = \frac{h_B\ (1\ +\ R_{3+})}{h_{total}}. \qquad (33)$$

Equations (31) and (33) provide two different methods to calculate Fe^{2+} subspectral areas: either using h_C and R_{2+} with equations (31) or using h_B and R_{3+} with equations (33) and (32).

Table 9
Relative amounts of Fe^{2+} and Fe^{3+} for the Temperature Series [a]

T[b]	Fe^{2+} / Fe_{total}	Fe^{3+} / Fe_{total}
426	.894 ± .015	.106 ± .015
598	.787 ± .015	.213 ± .015
650	.736 ± .006	.264 ± .006
661*	.519 ± .009	.481 ± .009
689	.480 ± .012	.520 ± .012
740	.233 ± .033	.767 ± .033
785	.191 ± .015	.809 ± .015
875	.161 ± .024	.839 ± .024

a. These results are based upon equations (31) and (32). The ratios of amounts are equal to the ratios of valence specific subspectral areas (see section 5.3)

b. Temperature ± 10 ^{0}C.

*. Heated for 94 instead of 24 hours.

Table 10
Relative amounts of Fe^{2+} and Fe^{3+} for the Time Series [a]

t [b]	Fe^{2+} / Fe_{total}	Fe^{3+} / Fe_{total}
0	.906 ± .030	.094 ± .030
.5	.897 ± .024	.103 ± .024
2	.763 ± .009	.237 ± .009
3	.671 ± .009	.329 ± .009
4	.599 ± .006	.401 ± .003
5	.540 ± .003	.460 ± .003
6	.513 ± .006	.487 ± .006
7	.477 ± .003	.523 ± .003
8	.435 ± .006	.565 ± .006
9	.420 ± .015	.580 ± .015
10	.405 ± .012	.595 ± .012
12	.373 ± .033	.627 ± .033
14	.352 ± .012	.648 ± .019
18	.298 ± .027	.702 ± .018

a. These results are based upon equations (31) and (32). The ratios of amounts are equal to the ratios of valence specific subspectral areas (see section 5.3)

b. Time in hours.

In tables 9 and 10 we list the relative amounts of Fe^{2+} (i.e. Fe^{2+}/Fe_{total}), and Fe^{3+} (i.e. Fe^{3+}/Fe_{total}), as calculated using equations (31) and (32) for the temperature and time series spectra, respectively. The associated uncertainties in the relative amounts are based upon the standard deviation errors for h_C/h_{total}.

Evaluation of the relative Fe^{2+} amounts by equation (31) produces systematically lower amounts for the temperature series spectra, than the relative Fe^{2+} amounts calculated by equations (32) and (33). In the case of the time series spectra, the opposite occurs. That is, the relative Fe^{2+} amounts are systematically lower by using equations (32) and (33) as compared to using equation (31). This is shown in tables 11 and 12. These systematic errors are within the random errors estimated for the relative Fe^{2+} amounts.

To verify the choice of the constants R_{2+} and R_{3+}, effective R_{3+} ($^{\#}R_{3+}$) and R_{2+} ($^{\#}R_{2+}$) values have also been evaluated for each spectrum (see tables 11 and 12). Except for $T \leq 650^0C$ in the temperature series and $t \leq 0.5$ hr. in the time series, the small variation in $^{\#}R_{3+}$ and $^{\#}R_{2+}$ suggests that $R_{2+} \approx 2$ and $R_{3+} \approx 0.6$ are robust values.

The effects of finite absorber thickness on the relative Fe^{2+}, and Fe^{3+}, amounts were estimated using a graphical technique described by

Table 11

Relative amounts of Fe^{2+} for the Temperature Series [a]

	R_{2+} = 1.981			R_{3+} = 0.623		
T[b]	Fe^{2+} / Fe_{total}		$^{a}R_{3+}$	Fe^{2+} / Fe_{total}		$^{a}R_{2+}$
426	.894	± .015	1.760	.937	± .016	2.129
598	.787	± .015	1.236	.849	± .013	2.197
650	.736	± .006	.881	.778	± .019	2.124
661*	.519	± .009	.643	.524	± .011	2.014
689	.480	± .012	.686	.498	± .015	2.102
740	.233	± .033	.649	.244	± .024	2.135
785	.191	± .015	.640	.193	± .023	2.113
875	.161	± .024	.628	.162	± .013	2.026

a. These results are based on calculations that use the mean spectral area of absorption peaks A, B, and C for each spectrum. The ratios of amounts are equal to the ratios of valence specific subspectral areas (see section 5.2)

b. Temperature ± 10°C.

* .Heated for 94 instead of 24 hours.

Table 12

Relative amounts of Fe^{2+} for the Time Series [a]

	R_{2+} = 1.981			R_{3+} = 0.623		
t[b]	Fe^{2+} / Fe_{total}		$^*R_{3+}$	Fe^{2+} / Fe_{total}		$^*R_{2+}$
0	.906	± .030	1.452	.940	± .010	2.082
.5	.897	± .024	1.215	.927	± .011	2.069
2	.763	± .009	.651	.766	± .011	1.997
3	.671	± .009	.580	.661	± .011	1.941
4	.599	± .006	.544	.583	± .003	1.880
5	.540	± .003	.615	.537	± .010	1.969
6	.513	± .006	.575	.497	± .008	1.894
7	.477	± .003	.631	.481	± .010	1.997
8	.435	± .006	.612	.430	± .010	1.954
9	.420	± .015	.579	.404	± .015	1.867
10	.405	± .012	.581	.390	± .013	1.865
12	.373	± .033	.591	.359	± .016	1.878
14	.352	± .010	.601	.338	± .017	1.904
18	.298	± .027	.588	.274	± .018	1.824

a. These results are based on calculations that use the mean spectral area of absorption peaks A, B, and C. The ratios of amounts are equal to the ratios of valence specific subspectral areas (see section 5.2)

b. Time in hours.

Rancourt et al (1992). Our thickest biotite sample measured 176 ± 3 μm thereby having n_a = 1.752 x 10^{18} ^{57}Fe atoms/cm^2 ± 2%. Based upon measured parameters, such as the physical thickness of the absorber, and constants like the average value of f_a for RT mica, we determined the thickness correction factor A/A_{th} as defined in section 4.4. In calculating the impact of thickness effects in this way, we found that the true Fe^{2+} amounts are ≤ 3% larger than the apparent Fe^{2+} amounts obtained directly from the spectral areas.

5.4 The degree of Fe^{2+} oxidation as a function of sample heating time and temperature

Within our given assumptions, we have established that it is possible to systematically oxidize Fe^{2+} into Fe^{3+} by incrementally heating our biotite sample for various times at various temperatures.

Figure 11 is a graph of the relative amounts of Fe^{2+} and Fe^{3+}, based on equations (31) and (32), versus annealing temperature for a 24 hour heating period. In the low temperature region (and up to 650° C) approximately 18% of the Fe^{2+} originally present in the biotite has been converted into Fe^{3+}. However, in the intermediate temperature region (650° C $\leq$ T $\leq$ 740°C), the relative amount of Fe^{2+} decreases by another 56% of the original Fe^{2+} amount as the temperature is increased. This suggests that in the intermediate temperature region there appears to be sufficient thermal energy available to drive the rate limiting step in the oxidation process. Even after our biotite has been annealed at 875°C, roughly 16% of the total Fe remains in the Fe^{2+} state.

The time dependence of the oxidation of Fe^{2+} in our biotite is documented in a graph of the relative amounts of Fe^{2+} and Fe^{3+} versus the heating time of the sample at 732° C (figure 12). Figure 12 suggests that the relative Fe^{2+} content in our biotite decreases exponentially as a function of

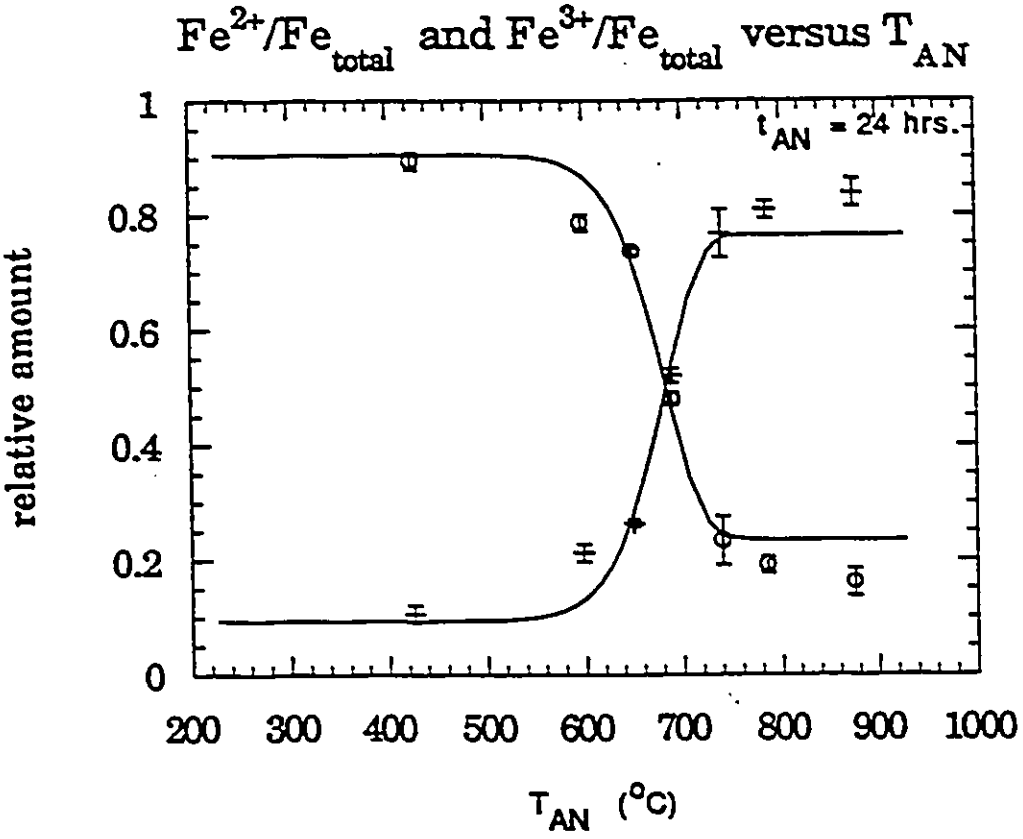

Fig 11 Relative amount of Fe^{2+} and Fe^{3+} versus annealing temperature (T_{AN}) for a 24 hour annealing time (t_{AN})

The open circles and the crosses represent the relative amounts of Fe^{2+} and Fe^{3+}, respectively. The solid line represents a fit using our modified one-step model. The relative amounts of Fe^{2+} and Fe^{3+} correspond to those given in table 11.

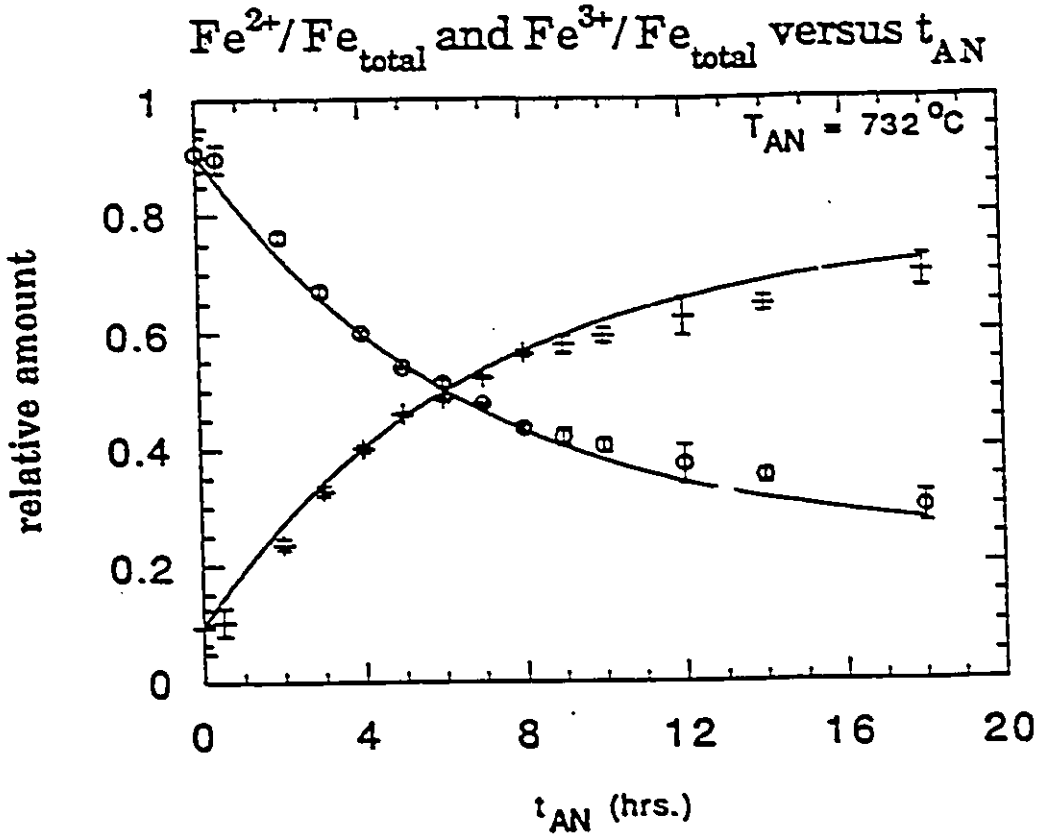

Fig 12 Relative amount of Fe^{2+} and Fe^{3+} versus annealing time (t_{AN}) at a sample heating temperature of 732°C.

The open circles and the crosses represent the relative amounts of Fe^{2+} and Fe^{3+}, respectively. The solid line represents a fit (the same as in figure 11) using our modified one-step model. The relative amounts of Fe^{2+} and Fe^{3+} correspond to those given in table 12.

sample heating time, as in equation (8).

To understand the combined time and temperature dependence of the Fe^{2+} oxidation process, two models were evaluated. The first model is based upon a simple activation process for Fe^{2+} oxidation, as outlined in section 2.2, and was tested by least squares adjustment. This simple model is unable to follow the measured time and temperature trends for the Fe^{2+} oxidation. A modification of the one-step model, which permits a finite amount ($N_{2+}^{\bullet}$) of Fe^{2+} to remain unoxidized, did reproduce the trends in annealing time and temperature. This modified one-step model, and its results are outlined below.

The modified one-step model may be written as:

$$N_{2+} = (N_{2+}^{\circ} - N_{2+}^{\bullet}) \exp(-ft) + N_{2+}^{\bullet} \quad (34)$$

$$N_{3+} = N_{3+}^{\circ} + (N_{2+}^{\circ} - N_{2+}^{\bullet})(1 - \exp(-ft)) \quad (35)$$

where the symbols have there previously defined meanings. In essence the modified one-step model substitutes equation (34) and (35) for equations (8) and (7) respectively. The conservation of the number of iron atoms (i.e. equation (9)) and the temperature dependence of f (i.e. equation (10)) remains the same in this modified model.

Simultaneously fitting this modified model to both the time and

temperature series (all spectra) gives an estimate of the bottleneck barrier energy (E_b), the bottleneck attempt frequency (f_o) and an unoxidized relative Fe^{2+} amount (N_{2+}^*). The resulting optimized parameters are:

$$E_b = 2.36 \begin{matrix} +0.01 \\ -0.02 \end{matrix} \text{ eV}$$

$$f_o = 2.91 \times 10^7 \begin{matrix} +7.8 \times 10^6 \\ -5.8 \times 10^6 \end{matrix} \text{ sec}^{-1}$$

$$N_{2+}^* = 0.236 \begin{matrix} +0.024 \\ -0.026 \end{matrix}$$

This particular least squares fit had a $\chi^2 = 126$ and 18 degrees of freedom (ν=18). The χ^2 was defined in the usual way with the weighting factors given by the inverse of the square of the uncertainties in the measured amounts. The errors assigned to E_b, f_o, and N_{2+}^* have been estimated by minimizing the modified model, with fixed values of N_{2+}^*, such that the χ^2 was approximately 1 standard deviation (s.d.=$\sqrt{(2\nu)}$) above the original χ^2.

The number of degrees of freedom (ν) for this model is much less

than the χ^2 ,which suggests that the modified model is probably incorrect for this data set (see section 3.4). It is nonetheless possible to interpret the results of this model in terms of the microscopic behaviour of the Fe^{2+} oxidation process.

According to our modified model, the dominant process in the oxidation of Fe^{2+} requires on the order of 10^7 attempts per second, and a kinetic energy of approximately 2 eV, to allow one Fe^{2+} oxidation event to occur. An event may be a combination of reactions or processes within the solid. For instance, an event could be the loss of one electron by Fe^{2+} to become Fe^{3+} in combination with the loss of hydrogen from the lattice due to the formation of water on the surface of the solid. It is not possible to determine the nature of these events from our preliminary analysis.

Given the composition of our biotite sample, it is possible that a finite amount of Fe^{2+} will remain unoxidized even after the sample is annealed at high temperature. This is incorporated in the modified model and is evident in the finite amount of Fe^{2+} present in the 875^{0}C sample. According to the chemical analysis of our biotite, there are almost an equal number of fluorine and chlorine ions as there are hydroxyl groups per structural formula of the biotite. Consequently, hydroxyl groups, that are part of the Fe^{2+} octahedra, may actually have been replaced by either fluorine or chlorine ions, thereby preventing some of the Fe^{2+} ions from oxidizing. Alternatively, oxidation of nearby Fe^{2+} ions may leave some Fe^{2+}

sites without the hydroxyl groups that are required for the Fe^{2+} oxidation process.

According to this study heating biotite in air will cause Fe^{2+} to oxidize into Fe^{3+} by reaction (6):

$$(Fe^{2+} + CH^{-})_{mica} \rightarrow (Fe^{3+} + O^{2-})_{mica} + H \qquad (6)$$

However the dissociation of structural hydroxyl may also be associated with dehydroxylation, which is simply written as:

$$(2\,OH^{-})_{mica} \rightarrow (O^{2-})_{mica} + H_2O \qquad (36).$$

Estimates of the microscopic barrier energy for a single dehydroxylation event are on the order of 2eV for silicates such as muscovite mica and kaolinite (Brindley et al, 1987; Redfern, 1987). This barrier energy is within the range of E_b that is predicted by our model of iron oxidation in biotite. This suggests that the dissociation of structural hydroxyl groups may be the key to the bottleneck in the Fe^{2+} oxidation process in biotite.

6 Conclusions

In summary, reliable Fe^{2+} and Fe^{3+} amounts can be calculated from a spectrum of a single-crystal biotite absorber. We achieve this using a self consistent method that assumes constant ion-specific ratios of low to high energy line areas for the Fe^{2+} and Fe^{3+} subspectral doublets. At normal γ-ray incidence, these ratios are found to be $R_{2+}= 2.0$ and $R_{3+}= 0.6$ for our biotite and its oxidized products.

Our room temperature ^{57}Fe Mössbauer study of an artificially oxidized single-crystal natural biotite indicates that the degree of controlled Fe^{2+} oxidation in the sample can be understood in terms of a simple activation model. This is supported by figures 11 and 12, which are graphs of relative Fe^{2+} and Fe^{3+} content versus the annealing time and temperature, respectively. These graphs show that the model follows the trend in the Fe^{2+} and Fe^{3+} oxidation curves.

Analyzing the Fe^{2+} oxidation process in terms of a modified one step activation model is equivalent to assuming that the relative amount of Fe^{2+} decreases exponentially as a function of time, but a finite amount of Fe^{2+} does not participate in the oxidation process. From figures 11 and 12, it is evident, however, that the modified model does not reproduce all the features in the variations of relative amounts of Fe^{2+} and Fe^{3+}, in particular at high temperature ($T>740^0C$, t=24hrs.) or longer times ($t \geq 9$hrs, $T=732^0C$).

The optimized parameters of the modified one step model indicate that the bottleneck step of the oxidation has a barrier energy (E_b) of $2.36^{+.01}_{-.02}$ eV, and requires on the order of $2.9\text{x}10^{7}{}^{+7.8\text{x}10^{6}}_{-5.8\text{x}10^{6}}$ sec^{-1} attempts per second (f_o) for one $Fe^{2+} \rightarrow Fe^{3+}$ event to occur in a time $t = \frac{1}{f} = \frac{\exp(\frac{+E_b}{k_b T})}{f_o}$. The unoxidizable relative amount of Fe^{2+} (N_{2+}^{*}) predicted by this model is $0.24 \pm .03$.

Our results do not contain the necessary information to conclusively determine the nature of the microscopic events involved in the overall oxidation. However, the effective one-step barrier energy obtained suggests that a dehydroxylation-like step is involved and represents the time bottleneck for the entire process.

References

Addison, C.C., Addison, W.E., Neal, G.H., Sharp, J.H. (1962) Amphiboles. Part 1. The oxidation of crocidolite, J. Chem. Soc., p.1468

Annersten, H. (1974) Mössbauer studies of natural biotites, Am. Mineral., vol 59, p. 143

Bailey, S.W., (Editor), (1984) Micas , Reviews in Mineralogy, Miner. Soc. of America, vol. 13

Bancroft, G.M., and Brown,J.R. (1975) A Mössbauer study of coexisting hornblendes and biotites: quantitative Fe^{3+}/Fe^{2+} ratios Am. Miner., vol 60, p.265

Brindley, G.W., and Lemaitre, J., (1987) Chemistry of clays and clay minerals, Miner. Soc. monograph no. 6, Longman, London

Deer, W.A., Howie, R.A., Zussman, J. (1966) An introduction to the rock forming minerals, Longman, London

Dyar, M.D. (1984) Precision and interlaboratory reproducibility of measurements of the Mössbauer effect in minerals, Am. Mineral., vol 14, p. 1127

Dyar, M.D. (1987) A review of Mössbauer data on trioctahedral micas: evidence for tetrahedral Fe^{3+} and cation ordering, Am. Mineral., vol 72, p. 102

Farmer, V.C., Russell, J.D., McHardy, W.J., Newman, A.C.D., Ahldrichs, J.L., Rimsaite, J.Y.H. (1971) Evidence for loss of protons and octahedral iron from oxidized biotites and vermiculites, Mineral. Mag., vol 38, p. 121

Gendler, T.S., Daynyak, L.G., Kuz'min, R.N., (1978) Parameters of the Mössbauer spectrum of Fe^{3+} ions in biotite, and continuity of biotite-oxybiotite transition at 300-900 K, Trans. from Geokhimiya, no. 11, p. 1633

Goodman, B.A., and Wilson, M.J. (1973) A study of the weathering of a biotite using the Mössbauer effect, Mineral. Mag., vol 39, p. 443

Greenwood, N.N., and Gibb, T.C. Mössbauer spectroscopy, Chapman and Hall, London, (1971)

Hargraves, P., Rancourt, D. G., Lalonde, A. E. (1990) Single-crystal Mössbauer study of phlogopite mica, Can. J. Phys., vol 68, p. 128

Hellner, E., and Euler, R. (1957) Geochimica Acta, vol 12, p.47, (not seen; extracted from Mineral. Mag., March 1975, vol 40, p.79)

Heller-Kallai, L., Rozenson, I. (1981) The use of Mössbauer spectroscopy of iron in clay mineralogy, Phys. Chem. Minerals, vol 7, p. 223

Hogg, C.S., and Meads, R.E. March (1975) A Mössbauer study of thermal decomposition of biotites, Mineral. Mag., vol 40, p. 79

James, F., and Roos, M. (1975) MINUIT- A system for function minimization and analysis of the parameter errors and correlations, Computer Phys. Comm. 10, p. 343, North-Holland Publishing Company

Mössbauer, R.L. (1958), Z. Physik, vol 151, p. 124 (not seen; extracted from Mössbauer spectroscopy and transition metal chemistry, Springer-Verlag, Berlin Heidelberg New York, (1978))

Press, W.H., Flannery, B.P., Teukolsky, S.A., Vetterling, W.T. Numerical Recipes- The art of scientific computing, Press Syndicate of the University of Cambridge, New York, (1988)

Rancourt, D.G. (1989) . Accurate site populations from Mössbauer spectroscopy, Nucl. Instrum. Methods Phys. Res. Sect. B, vol 44, p. 199

Rancourt, D.G., Dang Mei-Zhen, Lalonde, A.E. (1992) Mössbauer spectroscopy of tetrahedral Fe^{3+} in trioctahedral micas, Am. Mineral., vol 77, p. 34

Rancourt, D.G., McDonald, A.M., Lalonde, A.E., Ping, J.Y. (1992) Mössbauer absorber thickness for accurate site populations in iron-bearing minerals, in press, Am. Mineral.

Rancourt, D.G., Ping, J.Y. (1991) Voigt based methods for arbitrary-shape static hyperfine parameter distributions in Mössbauer spectroscopy, Nucl. Instrum. Methods Phys. Res. Sect. B, vol 58, p. 85

Redfern, S.A.T., (1987) The kinetics of dehydroxylation of kaolinite, Clay Miner., vol 22, p. 447

Rimsaite, J. (1970) Structural formulae of oxidized and hydroxyl-deficient micas and decomposition of the hydroxyl group, Contr. Mineral. and Petrol., vol 25, p. 225

Royer, M. (1991) Site specific ^{57}Fe Mössbauer recoiless fractions in true trioctahedral micas, M.Sc. thesis, University of Ottawa, Ottawa, Ont.

Tripathi, R.P., Chandra, U., Chandra, R., Lokanathan, S. (1978) A Mössbauer study of the effects of heating biotite, phlogopite, and vermiculite, J. Inogr. Nucl. Chem., vol 40, p. 1293

Vedder, W., and Wilkins, R.W.T. (1969) Dehydroxylation and rehydroxylation, oxidation and reduction in micas, Am. Mineral., vol 54, p. 482

Weisskopf, V., and Wigner, E. (1930) Z. Physik, vol 63, p54 and vol 65 p. 18 (not seen; extracted from Mössbauer spectroscopy and transition metal chemistry, Springer-Verlag, Berlin Heidelberg New York , (1978))

Zoltai, T., and Stout, J.H., Mineralogy concepts and principles, Burgess publishing company, Minneapolis, MN., (1984)

Appendix A

The following is a list of the tables of the optimized parameters for the various individual and multifits of the Temperature and Time series spectra that can be found in this appendix.

Individual 1-1-1 Fits of Temperature Series [a]

T[b]	σ_1[c]	h_1/h_{tot}[d]	V_1[c]	σ_2	h_2/h_{tot}	V_2
426	.145	.598	-.082	.370	.112	.424
598	.180	.545	-.064	.531	.194	.664
650	.184	.565	-.057	.375	.190	.865
661	.178	.534	-.039	.209	.289	.981
689	.175	.527	-.054	.210	.308	.980
740	.182	.462	-.087	.173	.454	1.000
785	.218	.444	-.134	.192	.490	1.016
875	.286	.434	-.162	.220	.473	1.013

T	σ_3[c]	h_3/h_{tot}[d]	V_3[c]	h_{tot}[c]	BG[c]	γ	χ^2_{red}
426	.134	.307	2.300	85654	441064	.233	.974
598	.170	.261	2.300	286668	1042800	.187	1.011
650	.166	.245	2.294	253745	1005730	.212	1.018
661	.131	.176	2.239	928259	3425219	.298	1.172
689	.124	.165	2.251	261381	1321936	.330	.675
740	.062	.085	2.168	171769	1270294	.424	.904
785	.103	.066	2.121	169842	759347	.406	1.417
875	.363	.093	1.936	188328	782902	.260	.970

a. Sample heated in air for 24 hours.
b. Temperature ± 10°C.
c. Gaussian width (σ_i), line position (V_i), and Lorentzian full width are in mm/sec.
d. (h_i/h_{tot}) is the ratio of the height of an individual line to the total of all Lorentzian heights for the spectrum.
e. The background and total Lorentzian height are in counts per channel.
•. Heated for 94 instead of 24 hours.

Individual 2-2-1 Fits of Temperature Series [a]

T[b]	σ_1[c]	h_1/h_{tot}[d]	V_1[c]	σ_2	h_2/h_{tot}	V_2
426	.108	.304	-.131	.122	.360	.148
598	.090	.177	-.139	.213	.446	.016
650	.067	.162	-.157	.184	.436	.014
661*	.156	.320	-.055	.208	.223	.005
689	.128	.258	-.072	.250	.283	-.015
740	.377	.216	-.227	.200	.243	-.032
785	.359	.240	-.260	.203	.212	-.050
875	.319	.377	-.195	.077	.065	-.057

T	σ_3	h_3/h_{tot}	V_3	σ_4	h_4/h_{tot}	V_4
426	.110†	.026	.875†	.706	.009	1.210†
598	.190	.115	.875†	.600	.007	1.210†
650	.343	.112	.927	.111	.004	.968
661*	.000	.013	.773	.188	.267	1.003
689	.014	.051	.791	.179	.243	1.043
740	.235	.368	.975	.609	.124	1.509
785	.203	.316	.945	.296	.171	1.244
875	.037	.069	.835	.217	.419	1.071

Individual 2-2-1 Fits of Temperature Series... continued [a]

T	σ_s	$h_{s/h_{tot}}$	V_s	h_{tot} [e]	BG [e]	γ [c]	χ^2_{red}
426	.141	.300	2.300†	90434	441084	.252	.520
598	.155	.255	2.300†	253744	1042826	.210	.561
650	.147	.249	2.294	206499	1005808	.266	.599
661*	.125	.177	2.239	887036	3425336	.312	1.169
689	.130	.165	2.250†	268507	1321923	.326	.590
740	.119	.049	2.197	396517	1269976	.174	.576
785	.148	.061	2.154	296683	759135	.224	.677
875	.244	.070	2.058	175179	782957	.282	.574

a. Sample heated in air for 24 hours.

b. Temperature = 10°C.

c. Gaussian width (σ_i), line position (V_i), and Lorentzian full width are in mm/sec.

d. (h_i/h_{tot}) is the ratio of the height of an individual line to the total of all Lorentzian heights for the spectrum.

e. The background and total Lorentzian height are in counts per channel.

*. Heated for 94 instead of 24 hours.

†. Parameter was fixed during fitting.

1-1-1 Multifit of Temperature Series [a]

T[b]	h_1/h_{tot}[c]	h_2/h_{tot}	h_3/h_{tot}	h_{tot}[d]	BG[d]
426	.673	.022	.305	69693	441276
598	.650	.079	.271	161284	1043261
650	.620	.129	.250	160955	1006113
661*	.537	.288	.175	796621	3426251
689	.530	.307	.163	245709	1321994
740	.448	.469	.083	192197	1269916
785	.423	.510	.067	180425	759348
875	.405	.543	.053	128581	782589

a. Sample heated in air for 24 hours. The Gaussian widths (σ_i) and line positions (V_i) for the repective Voigt lines. in mm/sec, are:

σ_1=.163, σ_2=.200, σ_3=.107.

V_1= -.052, V_2=1.000, and V_3=2.263

The multifit Lorentzian full width and the reduced chi-squared are:

$$\gamma = .360 \text{ mm/sec}, \text{and } \chi^2_{red} = 3.34$$

b. Temperature ± 10 °C.

c. ($h_{i/h_{tot}}$) is the ratio of height of an individual line to the total of all Lorentzian heights for the spectrum.

d. The background and total Lorentzian height are in counts per channel.

*. Heated for 94 instead of 24 hours.

2-1-2 Multifit of Temperature Series [a]

T[b]	h_1/h_{tot}	[c]h_2/h_{tot}	h_3/h_{tot}	h_4/h_{tot}	h_5/h_{tot}
426	.040	.617	.050	.064	.229
598	.025	.612	.100	.054	.209
650	.035	.572	.146	.071	.175
661*	.051	.476	.299	.096	.079
689	.129	.395	.314	.083	.079
740	.251	.203	.457	.086	.002
785	.435	.008	.485	.072	.000
875	.421	.008	.509	.063	.000

a. Sample heated in air for 24 hours.
The fixed Gaussian widths (σ_i) and fixed line positions (V_i) for the repective Voigt lines. in mm/sec, are:
σ_1=.277 , σ_2=.189 , σ_3=.247 , σ_4=.149 , σ_5=.120
V_1= -.151 , V_2=-.035 , V_3=.996 , V_4=2.154 , V_5=2.327
The multifit Lorentzian full width and the reduced chi-squared are:

$$\gamma = .240 \text{ mm/sec , and } \chi^2_{red} = 1.465$$

b. Temperature ± 10 °C.

c. (h_i/h_{tot}) is the ratio of the height of an individual line to the total of all Lorentzian heights for the spectrum.

d. The background and total Lorentzian height are in counts per channel.

*. Heated for 94 instead of 24 hours.

2-1-2 Multifit of Temperature Series continued [a)]

T	$h^{d)}_{tot}$	$BG^{d)}$
426	98725	441110
598	227283	1042897
650	227388	1005753
661*	1138626	3424827
689	355428	1321707
740	286538	1269836
785	273126	759025
875	198840	782807

2-2-1 Multifit of Temperature Series [a]

T[b]	h_1/h_{tot}	[c] h_2/h_{tot}	h_3/h_{tot}	h_4/h_{tot}	h_5/h_{tot}
426	.000	.663	.036	.000	.300
598	.000	.641	.091	.001	.268
650	.000	.612	.136	.006	.246
661*	.000	.527	.260	.046	.168
689	.048	.478	.270	.052	.153
740	.122	.330	.364	.117	.067
785	.182	.255	.362	.160	.041
875	.218	.205	.369	.177	.030

a. Sample heated in air for 24 hours.
The Gaussian widths (σ_i) and line positions (V_i) for the repective Voigt lines. in mm/sec, are:
σ_1=.292, σ_2=.189, σ_3=.209. σ_4=.461, σ_5=.143
V_1= -.354, V_2=-.040, V_3=.969, V_4=1.312, V_5=2.268
The multifit Lorentzian full width and the reduced chi-squared are:

$$\gamma = .260 \text{ mm/sec , and } \chi^2_{red} = 1.225$$

b. Temperature ± 10 °C.

c. (h_i/h_{tot}) is the ratio of the height of an individual line to the total of all Lorentzian heights for the spectrum.

d. The background and total Lorentzian height are in counts per channel.

*. Heated for 94 instead of 24 hours.

2-2-1 Multifit of Temperature Series continued [a)]

T	$h^{d)}_{tot}$	$BG^{d)}$
426	91255	441133
598	211060	1042932
650	210086	1005782
651	1051851	3424978
689	331037	1321779
740	271246	1270092
785	258937	759220
875	191955	782996

2-2-2 Multifit of Temperature Series [a]

T[b]	h_1/h_{tot} [c]	h_2/h_{tot}	h_3/h_{tot}	h_4/h_{tot}	h_5/h_{tot}
426	.033	.628	..042	.007	.054
598	.010	.630	.092	.004	.050
650	.027	.585	.129	.014	.068
661*	.045	.485	.268	.028	.093
689	.130	.398	.274	.038	.073
740	.253	.207	.374	.083	.080
785	.381	.066	.374	.116	.063
875	.433	.002	.371	.144	.050

a. Sample heated in air for 24 hours.
The Gaussian widths (σ_i) and line positions (V_i) for the repective Voigt lines, in mm/sec, are:
σ_1=.298, σ_2=.189, σ_3=.214, σ_4=.270, σ_5=.149†, σ_6=.120†
V_1= -.158, V_2=-.035, V_3=.959, V_4=1.309, V_5=2.154†, V_6=2.327†
The fixed multifit Lorentzian full width and it's reduced chi-squared are:

$$\gamma = .240 \text{ mm/sec , and } \chi^2_{red} = 1.100$$

b. Temperature ± 10 °C.

c. (h_i/h_{tot}) is the ratio of the height of an individual line to the total of all Lorentzian heights for the spectrum.

d. The background and total Lorentzian height are in counts per channel.

*. Heated for 94 instead of 24 hours.

†. Parameter fixed during fitting.

2-2-2 Multifit of Temperature Series continued [a)]

T	h_{6}/h_{tot}	$h^{d)}_{tot}$	$BG^{d)}$
426	.243	98369	441114
598	.214	226189	1042903
650	.177	225641	1005741
661*	.083	1134188	3424859
689	.088	356637	1321735
740	.002	288951	1269924
785	.000	276269	759994
875	.001	203962	782911

3-2-2 Multifit of Temperature Series [a]

T[b]	h_1/h_{tot}	[c]h_2/h_{tot}	h_3/h_{tot}	h_4/h_{tot}	h_5/h_{tot}
426	.000	.000	.660	.039	.000
598	.000	.000	.638	.079	.018
650	.000	.000	.608	.122	.023
661*	.000	.039	.494	.226	.068
689	.001	.103	.432	.221	.085
740	.094	.072	.298	.288	.167
785	.168	.040	.238	.274	.221
875	.220	.000	.208	.270	.253

a. Sample heated in air for 24 hours.
The Gaussian widths (σ_i) and line positions (V_i) for the repective Voigt lines. in mm/sec, are:
σ_1=.295, σ_2=.429, σ_3=.189. σ_4=.203, σ_5=.319, σ_6=.130, σ_7=.090
V_1=-.351, V_2=-.125, V_3=-.040, V_4=.953, V_5=1.146, V_6=2.167, V_7=2.364
The multifit Lorentzian full width and reduced chi-squared are:

$$\gamma = .244 \text{ mm/sec , and } \chi^2_{red} = .956$$

b. Temperature ± 10 °C.

c. (h_i/h_{tot}) is the ratio of the height of an individual line to the total of all Lorentzian heights for the spectrum.

d. The background and total Lorentzian height are in counts per channel.

*. Heated for 94 instead of 24 hours.

3-2-2 Multifit of Temperature Series continued [a]

T	h_{6}/h_{tot}	h_{7}/h_{tot}	$h^{d)}_{tot}$	$BG^{d)}$
426	.120	.181	96048	441098
598	.103	.163	222068	1042873
650	.106	.141	197463	1005722
661	.112	.062	1118166	3424941
689	.094	.065	351823	1321773
740	.074	.007	287055	1270049
785	.059	.000	272929	759147
875	.049	.000	200993	782905

1-1-1 Multifit of Time Series [a]

t[b]	h_1/h_{tot}[c]	h_2/h_{tot}	h_3/h_{tot}	h_{tot}[d]	BG[d]
0	.658	.033	.310	1067172	2802985
.5	.655	.043	.302	146823	391481
2	.602	.145	.253	301528	818696
3	.566	.210	.224	545445	1585664
4	.543	.258	.200	378012	996735
5	.529	.290	.181	328788	864460
6	.517	.312	.171	388773	1015115
7	.512	.328	.160	342588	893487
8	.499	.357	.145	322635	866694
9	.481	.378	.141	480493	1222434
10	.481	.384	.135	474969	1158232
12	.470	.406	.124	408449	1017985
14	.462	.419	.119	623003	1522228
18	.449	.452	.100	378660	968802

a. The Gaussian widths (σ_i) and line positions (V_i) for the repective Voigt lines. in mm/sec, are:

σ_1=.169, σ_2=.227, σ_3=.124.

V_1= -.045, V_2=.989, and V_3=2.279

The multifit Lorentzian full width and the mean reduced chi-squared are:

γ = .294 mm/sec , and χ^2_{red}=6.913

b. Time is in hours.

c. (h_i/h_{tot}) is the ratio of the height of an individual line to the total of all Lorentzian heights for the spectrum.

d. The background and total Lorentzian height are in counts per channel.

2-1-2 Multifit of Time Series [a]

t[b]	h_1/h_{tot} [c]	h_2/h_{tot}	h_3/h_{tot}	h_4/h_{tot}	h_5/h_{tot}
0	.052	.605	.053	.080	.210
.5	.108	.532	.079	.118	.163
2	.080	.514	.146	.095	.165
3	.057	.505	.216	.102	.120
4	.007	.532	.259	.097	.106
5	.097	.431	.290	.105	.077
6	.054	.463	.310	.096	.078
7	.115	.398	.325	.091	.071
8	.098	.404	.350	.095	.054
9	.189	.303	.365	.094	.049
10	.111	.374	.376	.095	.044
12	.157	.318	.392	.100	.033
14	.146	.323	.410	.092	.029
18	.189	.271	.435	.096	.010

a. The Gaussian widths (σ_i) and line positions (V_i) for the respective Voigt lines, in mm/sec, are:

σ_1=.277† , σ_2=.189† , σ_3=.247† , σ_4=.149† , σ_5=.120 †

V_1= -.151† , V_2=-.035† , V_3=.997† , V_4=2.154† , V_5=2.327†

The multifit Lorentzian full width and it's mean reduced chi-squared are:

γ = .240† mm/sec , χ^2_{red}= 4.220

b. Time is in hours.

c. (h_i/h_{tot}) is the ratio of the height of an individual line to the total of all Lorentzian heights for the spectrum.

d. The background and total Lorentzian height are in counts per channel .

†. Parameter fixed during fitting.

2-1-2 Multifit of Time Series continued [a]

t[b]	$h^{d)}_{tot}$	BG[d]
0	1291285	2802892
.5	187478	392190
2	374616	819085
3	666821	1585625
4	455954	996543
5	409356	864276
6	473693	1015037
7	420225	894056
8	396731	866721
9	603418	1223132
10	585870	1158320
12	516305	1019458
14	781292	1523257
18	474776	969071

2-2-2 Multifit of Time Series [a]

t[b]	h_1/h_{tot}[c]	h_2/h_{tot}	h_3/h_{tot}	h_4/h_{tot}	h_5/h_{tot}
0	.001	.651	.044	.000	.064
.5	.000	.645	.052	.000	.081
2	.001	.595	.145	.004	.092
3	.037	.529	.188	.022	.088
4	.057	.489	.227	.027	.099
5	.104	.433	.249	.032	.085
6	.096	.431	.261	.042	.094
7	.120	.404	.267	.048	.098
8	.130	.385	.287	.055	.091
9	.133	.365	.305	.052	.110
10	.139	.360	.307	.058	.091
12	.154	.338	.321	.061	.096
14	.181	.308	.329	.066	.087
18	.190	.288	.345	.078	.086

a. The Gaussian widths (σ_i) and line positions (V_i) for the repective Voigt lines, in mm/sec, are:

σ_1=.413, σ_2=.183, σ_3=.215, σ_4=.259, σ_5=.153, σ_6=.118

V_1=-.158†, V_2=-.035†, V_3=.959†, V_4=1.309†, V_5=2.154†, V_6=2.327†

The multifit Lorentzian full width and the mean reduced chi-squared are:

γ = .221 mm/sec χ^2_{red}=2.120

b. Time is in hours.

c. (h_i/h_{tot}) is the ratio of the height of an individual line to the total of all Lorentzian heights for the spectrum.

d. The background and total Lorentzian height are in counts per channel.

†. Parameter fixed during fitting.

2-2-2 Multifit of Time Series continued [a]

t[b]	h_{6}/h_{tot}	h^{d}_{tot}	BG[d]
0	.241	1348266	2801368
.5	.212	185969	391259
2	.163	382039	818275
3	.137	702199	1585072
4	.101	491333	996479
5	.096	433295	864498
6	.076	513732	1015059
7	.062	459810	893549
8	.054	432538	866787
9	.035	648658	1222875
10	.045	639785	1158436
12	.029	553828	1018253
14	.028	850928	1522851
18	.015	521652	969238

3-2-2 Multifit of Time Series [a]

t[b]	h_1/h_{tot}[c]	h_2/h_{tot}	h_3/h_{tot}	h_4/h_{tot}	h_5/h_{tot}
0	.162	.152	.341	.033	.000
.5	.115	.060	.478	.039	.000
2	.036	.498	.078	.131	.003
3	.038	.159	.375	.192	.008
4	.002	.219	.303	.235	.019
5	.024	.337	.181	.257	.022
6	.011	.455	.048	.263	.051
7	.014	.419	.092	.287	.031
8	.004	.447	.049	.291	.065
9	.016	.404	.075	.329	.040
10	.002	.301	.184	.329	.051
12	.001	.483	.000	.352	.048
14	.001	.478	.001	.370	.038
18	.002	.452	.007	.387	.058

a. The Gaussian widths (σ_i) and line positions (V_i) for the repective Voigt lines, in mm/sec, are:

σ_1=.0003, σ_2=.196, σ_3=.156, σ_4=.189, σ_5=.325, σ_6=.113, σ_7=.041

V_1=-.123, V_2=-.041, V_3=-.008, V_4=.969, V_5=1.431, V_6=2.213, V_7=2.379

The multifit Lorentzian full width and it's reduced chi-squared are:

$$\gamma = .306 \text{ mm/sec , and mean } \chi^2_{red} = 5.374$$

b. Time is in hours.

c. (h_i/h_{tot}) is the ratio of the height of an individual line to the total of all Lorentzian heights for the spectrum.

d. The background and total Lorentzian height are in counts per channel.

3-2-2 Multifit of Time Series continued [a]

t[b]	h_6/h_{tot}	h_7/h_{tot}	h^{d}_{tot}	BG[d]
0	.163	.149	1026289	2802911
.5	.174	.135	140328	391440
2	.171	.085	297685	818912
3	.158	.070	525935	1585583
4	.149	.053	378204	998171
5	.145	.035	322396	894549
6	.141	.032	419419	1019974
7	.142	.016	335570	893611
8	.115	.030	337613	869208
9	.136	.000	471353	1222675
10	.132	.000	472467	1159000
12	.117	.000	402680	1018201
14	.118	.000	710928	1522799
18	.093	.000	375666	969174

Peak areas for the fits used in obtaining R_{2+} and R_{3+} *

2-1-2 Individual fit of the t=0hr. spectrum[a)]

$\frac{h_1}{h_{tot}}$[b)]	$\frac{h_2}{h_{tot}}$	$\frac{h_3}{h_{tot}}$	$\frac{h_4}{h_{tot}}$	$\frac{h_5}{h_{tot}}$	h_{tot}[c)]	BG[c)]
.289	.355	.044	.060	.251	12471257	2801456

a. The Gaussian widths (σ_i) and line positions (V_i) for the respective Voigt lines, in mm/s, are:

$\sigma_1 = .076$, $\sigma_2 = .153$, $\sigma_3 = .201$, $\sigma_4 = .149$†, $\sigma_5 = .119$†

$V_1 = -.152$, $V_2 = .065$, $V_3 = .811$, $V_4 = 2.154$†, $V_5 = 2.327$†

The Lorentzian full width, and it's reduced chi-squared are:

$\gamma = .240$† mm/sec, $\chi^2 = 1.807$.

b. ($\frac{h_i}{h_{tot}}$) is the ratio of the height of an individual line to the total of all Lorentzian heights for the spectrum.

c. The background and total Lorentzian height are in counts per channel.

†. Parameter fixed during fitting.

*. see section 5.3

Peak areas for the fits used in obtaining R_{2+} and R_{3+} ...continued

4-2-2 Individual fit of the 875 ^{0}C spectrum [a]

$\frac{h_1}{h_{tot}}$ [b]	$\frac{h_2}{h_{tot}}$	$\frac{h_3}{h_{tot}}$	$\frac{h_4}{h_{tot}}$	$\frac{h_5}{h_{tot}}$	$\frac{h_6}{h_{tot}}$
.127	.008	.288	.007	.383	.133

$\frac{h_7}{h_{tot}}$	$\frac{h_8}{h_{tot}}$	h_{tot}	BG
.053	.001	204695	782918

a. The Gaussian widths (σ_i) and line positions (V_i) for the respective Voigt lines, in mm/s, are:

σ_1 = .270†, σ_2 = .120†, σ_3 = .214†, σ_4 = .149†, σ_5 = .214†, σ_6 = .270†, σ_7 = .149†

σ_8 = .120†, V_1 = -.490, V_2 = -.108†, V_3 = -.082, V_4 = -.082†, V_5 = .959†, V_6 = 1.309

V_7 = 2.154†, V_8 = 2.327†

The Lorentzian full width, and it's reduced chi-squared are:

γ = .240† mm/sec, χ^2 = .630.

b. ($\frac{h_i}{h_{tot}}$) is the ratio of the height of an individual line to the total of all Lorentzian heights for the spectrum.

c. The background and total Lorentzian height are in counts per channel.

†. Parameter fixed during fitting.